Final Report for the Field-Reversed Configuration Power Plant Critical-Issue Scoping Study

J.F. Santarius, E.A. Mogahed, G.A. Emmert,
H.Y. Khater, C.N. Nguyen, S.V. Ryzhkov, M.D. Stubna,
L.C. Steinhauer, G.H. Miley

March 2000

UWFDM-1129

FUSION TECHNOLOGY INSTITUTE

UNIVERSITY OF WISCONSIN

MADISON WISCONSIN

Final Report for the
Field-Reversed Configuration Power Plant
Critical-Issue Scoping Study

Project DE-FG02-97ER54431

September 1, 1997—December 31, 1999

John F. Santarius, Elsayed A. Mogahed, Gilbert A. Emmert, Hesham Y. Khater, Canh N. Nguyen,[†] Sergei V. Ryzhkov,[‡] and Michael D. Stubna[#]

Fusion Technology Institute
Department of Engineering Physics
University of Wisconsin-Madison
1500 Engineering Drive
Madison, WI 53706

Loren C. Steinhauer
University of Washington

George H. Miley
University of Illinois

March 2000

UWFDM-1129

[†] Present address: Lehigh University
[‡] Present address: Bauman Moscow State Technical University
[#] Present address: Penn State University

Table of Contents

List of Figures

List of Tables

1 Introduction

1.1 Project activities

This report describes research in which a team from the Universities of Wisconsin, Washington, and Illinois performed a scoping study of critical issues for field-reversed configuration (FRC) power plants. The key tasks for this research were

1. *Systems analysis of deuterium-tritium (D-T) FRC fusion power plants*

2. *Conceptual design of the blanket and shield module for an FRC fusion core.*

The effort of approximately one-third of a full time equivalent (FTE) professional researcher per year was split among the participating institutions as follows: University of Wisconsin (70%), University of Washington (20%), and University of Illinois (10%).

1.1.1 Systems analysis and fusion core conceptual design

In order to perform the systems analysis, the University of Wisconsin's fusion power plant systems code, described in detail in Section 3, was modified from its initial form as a tokamak systems code to include FRC physics and engineering models. Some alternate modes of operation were also explored. The reference case and a case generated assuming liquid walls and very high power density are given in Section 4.

A key thrust of the research was to investigate a crucial question for FRC power plants:

> *Given success in the physics, would the engineering features of the resulting device be attractive?*

For the engineering conceptual design of the FRC fusion core, therefore, the project team focused on intermediate-term technology. For example, one decision was to use steel structure instead of exotic but relatively undeveloped materials, such as vanadium or silicon carbide. The FRC does indeed appear to lead to an attractive fusion power plant, based on several features of the design, including modest size, cylindrical symmetry, good thermal efficiency, and relatively easy maintenance. The resulting compact FRC fusion core of the reference case conceptual design possesses a high ratio of electric power to fusion core mass, indicating that it would certainly have favorable economics. Details of the design are discussed in Section 2.

1.1.2 Talks and poster papers

Table 1-1 lists the talks that project team members have given that are either directly or indirectly related to this research. Similarly, Table 1-2 lists related poster papers.

Table 1-1: Related Talks Given by D-T FRC Scoping Study Research Team Members.

Date	Speaker	Title	Meeting	Location
18-20 March 1998	Santarius	FRC Power Plants—a Fusion Development Perspective	US-Japan Workshop on Physics of High-Beta Fusion Plasmas	Univ. of Washington, Seattle, Washington
24-27 March 1998	Miley	On Design and Development Issues for the FRC and Related Alternate Confinement Concepts	IAEA Technical Committee Meeting on Fusion Power Plant Design	UKAEA, Culham, UK
27-31 July 1998	Steinhauer	FRC Plasma-Liquid Wall Physics Interface Issues§	APEX/ALPS Meeting	Sandia National Laboratory, Albuquerque, New Mexico
27-31 July 1998	Santarius	Field-Reversed Configuration Engineering Issues for Designs with Liquid Walls§	APEX/ALPS Meeting	Sandia National Laboratory, Albuquerque, New Mexico
2 Nov. 1998	Santarius	Field-Reversed Configuration Power Plants	University of Wisconsin Plasma Seminar	Univ. of Wisconsin, Madison, Wisconsin
Nov. 1998	Miley	On Design and Development Issues for the FRC	American Nuclear Society Meeting	
16-18 Feb. 1999	Moir (for Santarius)	Compact Toroid Fueling and Current Drive for Liquid-Walled FRC's§	APEX Project Meeting	UCLA, Los Angeles, California
8-9 June 1999	Santarius	Field-Reversed Configuration Fusion Power Plants	Workshop on Status and Promising Directions for Field-Reversed Configuration Research	PPPL, Princeton, New Jersey
13 Sept. 1999	Santarius	Field-Reversed Configurations	University of Wisconsin Plasma Seminar	Madison, Wisconsin
15-19 Oct. 2000	Mogahed	A Helium Cooled Li_2O Pebble Bed Blanket Design for Cylindrical Geometry	American Nuclear Society Topical Meeting on the Technology of Fusion Energy	Park City, Utah

§ Related, but not funded or only partially funded by the present research project.

Table 1-2: Related Poster Papers Given by D-T FRC Scoping Study Research Team Members.

Date	Authors	Title	Meeting	Location
7-11 June 1998	Santarius, Emmert, Khater, Mogahed, Nguyen, Steinhauer, Miley	Field-Reversed Power Plant Critical Issues	American Nuclear Society Topical Meeting on the Technology of Fusion Energy	Nashville, Tennessee
16-20 Nov. 1998	Nguyen, Santarius, Emmert, Ryzhkov, Stubna, Steinhauer	Commercial D-T FRC Power Plant Systems Analysis	American Physical Society Division of Plasma Physics Meeting	New Orleans, Louisiana
15-19 Nov. 1999	Santarius, Ryzhkov, Nguyen, Emmert, Steinhauer	Systems Analysis of D-T and D-^{3}He FRC Power Plants[§]	American Physical Society Division of Plasma Physics Meeting	Seattle, Washington

1.1.3 Papers

The following papers directly related to this research project have been published or are in progress:

1. J.F. Santarius, G.A. Emmert, H.Y. Khater, E.A. Mogahed, C.N. Nguyen, L.C. Steinhauer, and G.H. Miley, “Field-Reversed Configuration Power Plant Critical Issues,” University of Wisconsin Fusion Technology Institute Report UWFDM-1084 (June 1998).

2. E.A. Mogahed, H.Y. Khater, and J.F. Santarius, “A Helium Cooled Li_2O Pebble Bed Blanket Design for Cylindrical Geometry,” (prepared for ANS Topical Meeting on the Technology of Fusion Energy; thereby submitted to Fusion Technology, 2000).

3. C.N. Nguyen, J.F. Santarius, L.C. Steinhauer, and G.A. Emmert, “Systems Analysis of a D-T Field-Reversed Configuration Power Plant,” (in progress, 2000).

[§] Related, but not funded or only partially funded by the present research project.

The following papers, related to the research project but less closely so than the previously listed papers, grew out of the funded research or were activities mutually leveraged by the project (see Sec. 1.1.4):

1. R. W. Moir, T. D. Rognlien, K. Gulec, P. Fogarty, B. Nelson, M. Ohnishi, M. Rensink, J. F. Santarius, D. K. Sze, "Thick Liquid-walled, Field-reversed Configuration (FRC)," (prepared for ANS Topical Meeting on the Technology of Fusion Energy; thereby submitted to Fusion Technology, 2000).

2. S.V. Ryzhkov, J.F. Santarius, G.A. Emmert, C.N. Nguyen, and L.C. Steinhauer, "Systems Analysis of a D-^{3}He Field-Reversed Configuration Power Plant," (in progress, 2000).

3. J.F. Santarius, "Field-Reversed Configurations for Space Propulsion," (submitted to 31st AIAA Plasmadynamics and Lasers Conference, 19-22 June 2000, Denver, Colorado, paper AIAA-2000-2269).

1.1.4 Leveraged activities

Significant leverage for and by this project was gained by several activities not directly funded as part of the initial proposal. These leveraged activities included:

1. Canh N. Nguyen, a graduate student of Prof. Gilbert A. Emmert at the University of Wisconsin, joined the project with a UW Advanced Opportunities Fellowship that fully supported his part of the research project during his first academic year (1997-1998). The project then supported him for his second academic year. He provided most of the effort in converting the C version of the WISC program from a purely tokamak code into a code that also modeled the FRC.

2. Michael D. Stubna worked for two months during the summer of 1998 on the project at the University of Wisconsin with funding from a National Undergraduate Fellowship in Plasma Physics and Fusion Engineering. He began conversion of the WISC program from the C language to the Mathematica language. The C version of the program provided most of the information contained in this report. The Mathematica version, however, gives much more flexibility and readability to the program and, after further modification and extension by the University of Wisconsin PI (JFS) after the present grant expired, has become the primary version of the code.

3. Sergei V. Ryzhkov, a graduate student of Prof. Vladimir I. Khvesyuk at Bauman Moscow State Technical University, Moscow, Russia, joined the group for ten months during 1998-1999. He came to the U.S. specifically to study D-^{3}He fusion with the University of Wisconsin PI and was supported by the Russian President's Foundation, not the present research project. His participation, which consisted partly of modifying the WISC program to include D-^{3}He fuel for FRCs, enhanced the ability of the team to take a broader perspective on FRC development. He also examined the FRC energy confinement database and developed a new energy confinement scaling relation.

4. During FY99, the Advanced Power Extraction Project (APEX), led by Prof. Mohamed Abdou, UCLA, funded an effort of ~0.11 FTE by the University of Wisconsin PI to examine liquid-walled D-T FRC power plants.

5. During FY00, Dr. Francis Thio, NASA Marshall Space Flight Center, funded an effort of ~0.17 FTE by the University of Wisconsin PI to investigate FRCs for space propulsion.

1.1.5 Student involvement

This project educated three students. Section 1.1.4 describes their roles in the project, and Table 1-3 lists their present location.

Table 1-3: Students Educated during the D-T FRC Power Plant Critical-Issue Scoping Study.

Student	UW Degree	Present Location
Canh N. Nguyen	M.S. 1999	Lehigh University Graduate School
Sergei V. Ryzhkov	---	Bauman Moscow State Technical University Graduate School
Michael D. Stubna	---	Penn State University Graduate School

1.1.6 Recommendations for future FRC power plant research

Although the present research project investigated several interesting aspects of FRC power plant design that turned out to be attractive, many pathways remain unexplored for lack of resources. Recommendations for future FRC power plant research include:

1. ***The cylindrically symmetric geometry of FRC fusion cores allows the design of an attractive first-wall/blanket/shield/magnet module with reasonable engineering assumptions. The concept presented in this report should be pursued further for the FRC and other amenable configurations, such as the spheromak and spherical torus.***

2. ***Field-reversed configurations show promise for providing the most attractive performance of any magnetic fusion concept, and a detailed, integrated, conceptual design of a D-T FRC power plant should be undertaken at the level of at least 10 FTE's per year for two years.***

3. ***The geometry of FRC fusion cores fits the use of liquid walls very well, and the combination should be investigated in more depth.***

4. ***The FRC appears well suited to burning D-^{3}He fuel, and a detailed conceptual design at several FTE's per year for two years should be performed in order to assess whether such a device could achieve the watershed level of sufficiently attractive economics to break into the electricity market.***

5. ***Other applications of FRC devices should be scrutinized, particularly hydrogen production and space propulsion.***

1.2 Overview

An excellent balance between potential reactor attractiveness and technical development risk motivates the study of field-reversed configuration (FRC) power plants. The linear, cylindrical FRC geometry facilitates the design of tritium-breeding blankets, shields, magnets, and input-power systems, while the high FRC β (≡plasma pressure/magnetic field pressure) increases the plasma power density and allows a compact fusion core. The surface heat flux is moderate despite a high power density, however, because the plasma flowing to the end chamber walls carries much of the fusion power, as shown in Figure 1-1.

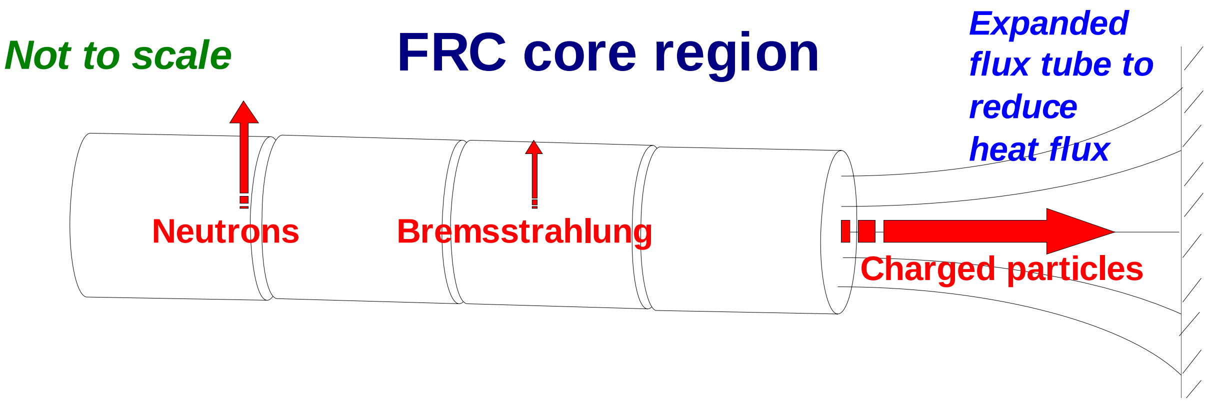

Figure 1-1: Energy flow from the FRC fusion core.

Encouraging recent physics progress by the small worldwide FRC research community has enhanced the prospects for successful FRC development.[1-3] Highlights include indications that natural minimum-energy FRC states exist,[4] stable operation at moderate s (plasma radius/average gyroradius),[5] startup by merging two spheromaks to form an FRC,[6] theoretically efficient current drive by rotating magnetic fields,[7] and an attractive Japanese D-^{3}He FRC power plant design.[8]

From an engineering standpoint, an FRC burning D-T fuel appears capable of being built largely with near-term technology. The main exceptions are the materials used for the first wall, blanket, and shield, which will be subject to high neutron fluences with consequent radiation damage and activation. If the more difficult physics requirements of D-^{3}He fuel could be achieved, essentially all necessary FRC technology appears to be in hand, benefits would be gained from direct conversion, and environmental and safety characteristics would be substantially improved.[9] Although both D-T and D-^{3}He fuels appear likely to perform well in FRC power plants, the focus of the present project has been on D-T fuel.

The FRC is an ellipsoidal magnetic configuration with no toroidal component immersed inside the magnetic field lines of an open-ended geometry. The FRC reactor is cylindrical, which would simplify much of the maintenance involved. The open field lines guide charged particles toward the ends for possible direct conversion as well as effectively removing impurities from the system. Because of the scaling of the fusion power density, $P/V \propto \beta^2 B^4$, the FRC can be an extremely high power density system.

Details of fusion core engineering, including a high-performance cylindrical blanket and shield concept, are discussed in Section 2. The physics and engineering models plus other aspects of the University of Wisconsin's power-plant systems code, WISC (WIsconsin Systems

Code), are discussed in Section 3. Section 4 of this report describes the study's reference FRC power plant case plus an interesting case with liquid walls.

1.3 References for Section 1

1. L.C. Steinhauer, et al., "FRC 2000: A White Paper on FRC Development in the Next Five Years," *Fusion Technology* **30**, 116 (1996).

2. A.L. Hoffman, L.N. Carey, E.A. Crawford, D.G.Harding, et al., "The Large-s Field-Reversed Configuration Experiment," *Fusion Technology* **23**, 185 (1993).

3. M. Tuszewski, "Field Reversed Configurations," *Nuclear Fusion* **28**, 2033 (1988).

4. L.C. Steinhauer and A. Ishida, "Relaxation of a Two-Species Magnetofluid and Application to Finite-β Flowing Plasmas," *Physics of Plasmas* **5**, 2609 (1998).

5. A.L. Hoffman, L.N. Carey, E.A. Crawford, D.G.Harding, et al., "The Large-s Field-Reversed Configuration Experiment," *Fusion Technology* **23**, 185 (1993).

6. M. Yamada, H. Ji, S. Hsu, T. Carter, R. Kulsrud, et al., "Study of Driven Magnetic Reconnection in a Laboratory Plasma," *Physics of Plasmas* **4**, 1936 (1997).

7. A.L. Hoffman, "Flux Buildup in Field Reversed Configurations Using Rotating Magnetic Fields," *Physics of Plasmas* **5**, 979 (1998).

8. H. Momota, A. Ishida, Y. Kohzaki, G.H. Miley, S. Ohi, et al., "Conceptual Design of the D-^{3}He Reactor ARTEMIS," *Fusion Technology* **21**, 2307 (1992).

9. J.F. Santarius, G.L. Kulcinski, L.A. El-Guebaly, and H.Y. Khater, "Could Advanced Fusion Fuels Be Used with Today's Technology?", *Journal of Fusion Energy* **17**, 33 (1998).

2 Fusion Core Engineering

2.1 The thermo-mechanical design of the first wall and blanket of the FRC

A helium-cooled solid breeder (Li_2O) has been chosen for the FRC first wall and blanket. Oxide-dispersion strengthened (ODS) ferritic steel (developed at Oak Ridge National Lab (ORNL)) is the advanced structural material considered for the reactor components. This new material is exceptionally creep-resistant compared with low activation ferritic-martensitic (FM) steels at temperatures above 600°C. At Oak Ridge National Lab, the advanced material program is considering an alternative approach to developing dispersion-strengthened alloys with enhanced high-temperature creep resistance.[1] A new alloy designated A21 is being developed. The alloy is based on a Fe-Cr-Co-Ni-Mo-Ti-C composition. Initial property measurements show that while the yield strength of A21 is only slightly higher than that of conventional low-activation steel, the creep strength over the range 600°C to 700°C is greatly improved over modified 9Cr-1Mo steel (T-91). Initial property measurements show that, at 650°C, the 10,000-hr rupture stress for the new steel is ≈100 MPa compared to ≈15 MPa for conventional 9Cr-1Mo steel.[2] Figure 2-1 shows the ultimate tensile strength of some low activation steel alloys versus temperature. The general performance indicates a sudden reduction in strength between 850 K and 925 K.

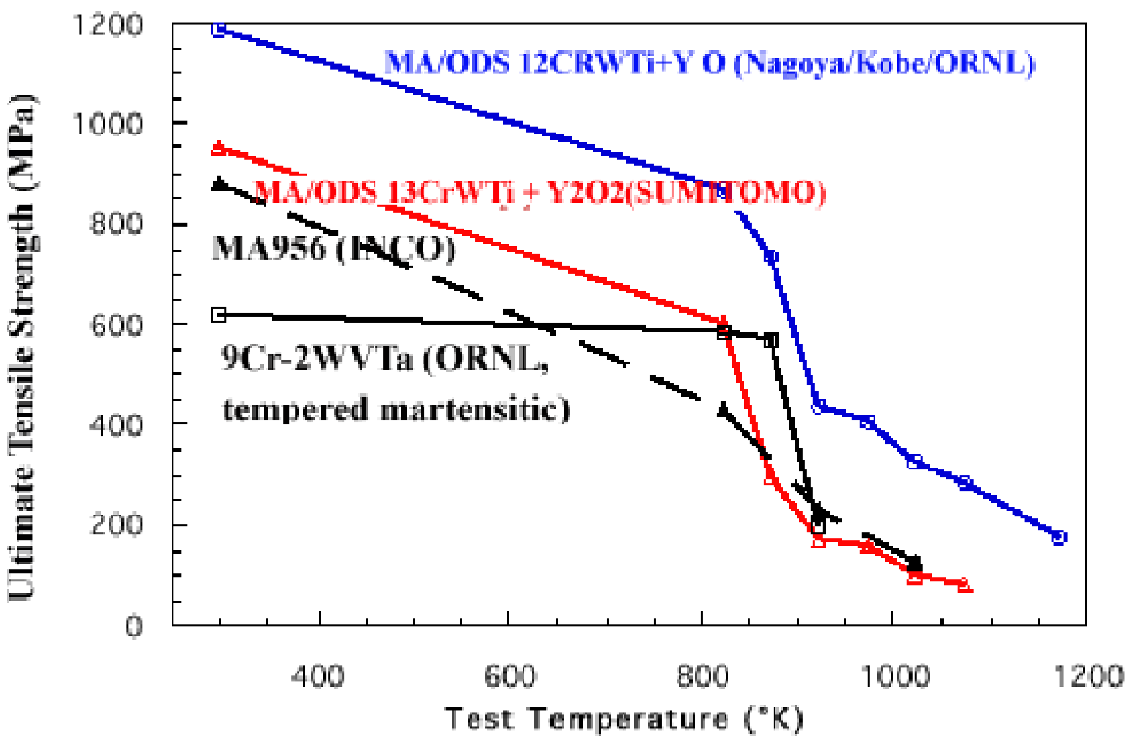

Figure 2-1: Comparison of the temperature-dependent tensile strengths of oxide dispersion strengthened and ferritic-martensitic (9Cr-2VTaW) steels.

The FRC design is modular with a length/module of 2.5 m. The total number of modules is 10. The solid breeder is Li_2O in the shape of tubes of 90% theoretical density. The cylindrical geometry of the FRC blanket (unlike the tokamak blanket) allows straight Li_2O tubes to be used. The coolant and the purge gas is helium at an average pressure of 18 MPa. In the first zone a single size Li_2O tube is used. The blanket consists of two zones, blanket-I and blanket-II, separated by two rows of steel tubes. The size of the Li_2O tubes in different zones is determined mainly by the temperature limits on the Li_2O solid breeder. The recommended maximum allowable temperature of the Li_2O solid breeder is 1000°C for sintering and the minimum allowable temperature is 400°C for tritium retention. The maximum temperature at the Li_2O tubes at any location of the reactor is determined from the thermal-hydraulics of the specific Li_2O tube zone. The steady state nuclear heating in the different zones is calculated with an average neutron wall loading of 5 MW/m^2. The surface heat flux is 0.2 MW/m^2. Figure 2-2 shows a sketch of the radial build (used in nuclear calculations) of the FRC concept with the distribution of the constituents of each component and the corresponding average nuclear heating in each zone.

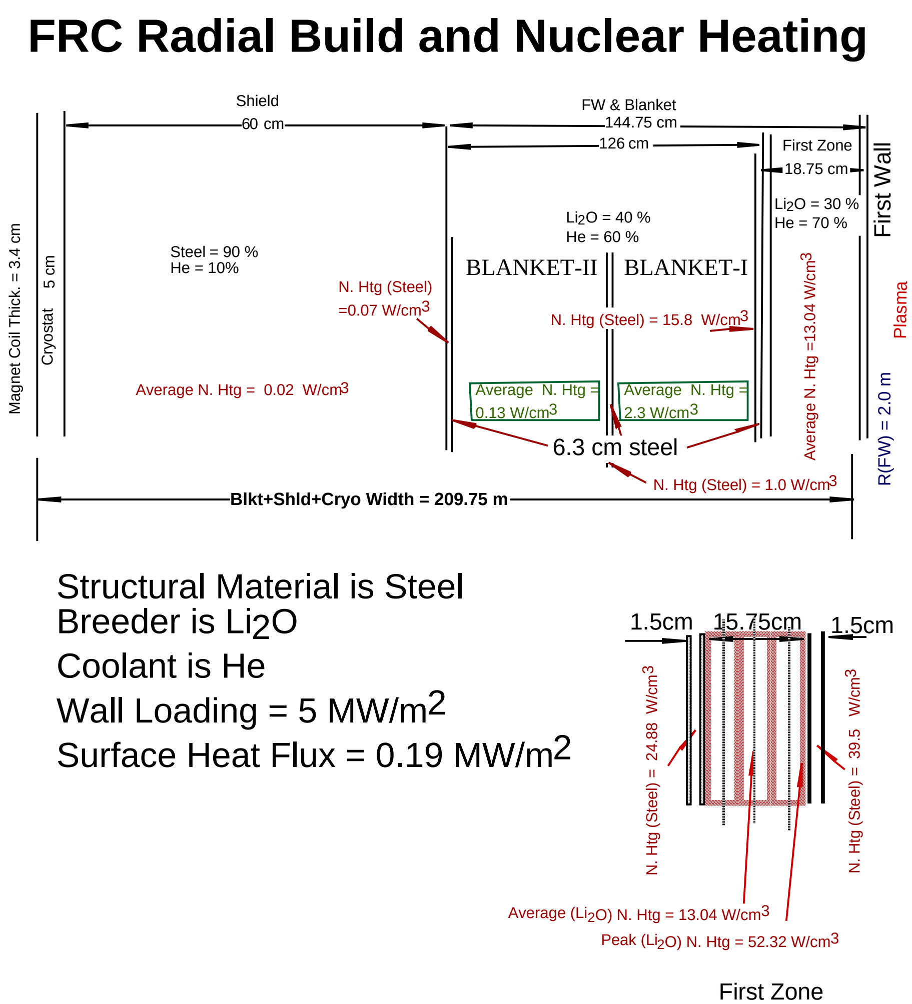

Figure 2-2: A sketch of the radial build of the FRC and nuclear heating in each zone.

2.2 The mechanical design of the first wall and blanket of the FRC

The first zone and the outward consecutive layers of the blanket are made of concentric cylinders with the plasma in the center. Figure 2-3 shows a sketch of the FRC cylindrical zones. The first zone consists of a first wall and a back wall made of steel cooled with helium and the space between them is filled with Li_2O tubes also cooled with helium. All the tubes run longitudinally and have a circular cross section. Figure 2-4 shows a detail of the first zone. The inner diameter of the steel tubes is 1 cm and the outer diameter is 1.5 cm. The inner diameter of the Li_2O tubes is 1.9 cm and the outer diameter is 3.15 cm. The ratio of Li_2O to helium is 30% to 70%.

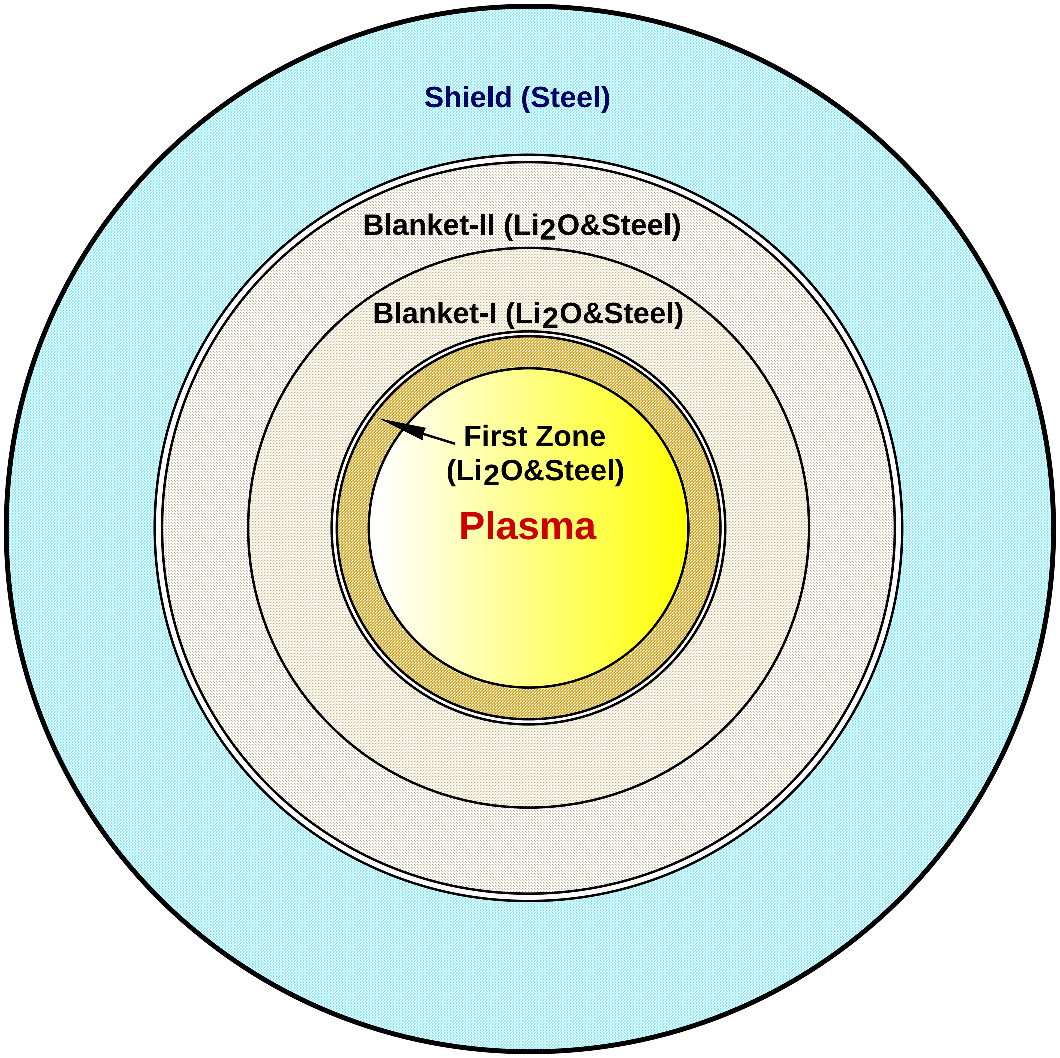

Figure 2-3: The FRC consists of concentric cylinders with the plasma in the core. The inner diameter of the first wall is 4.0 m. The outer diameter of the shield is 8.08 m.

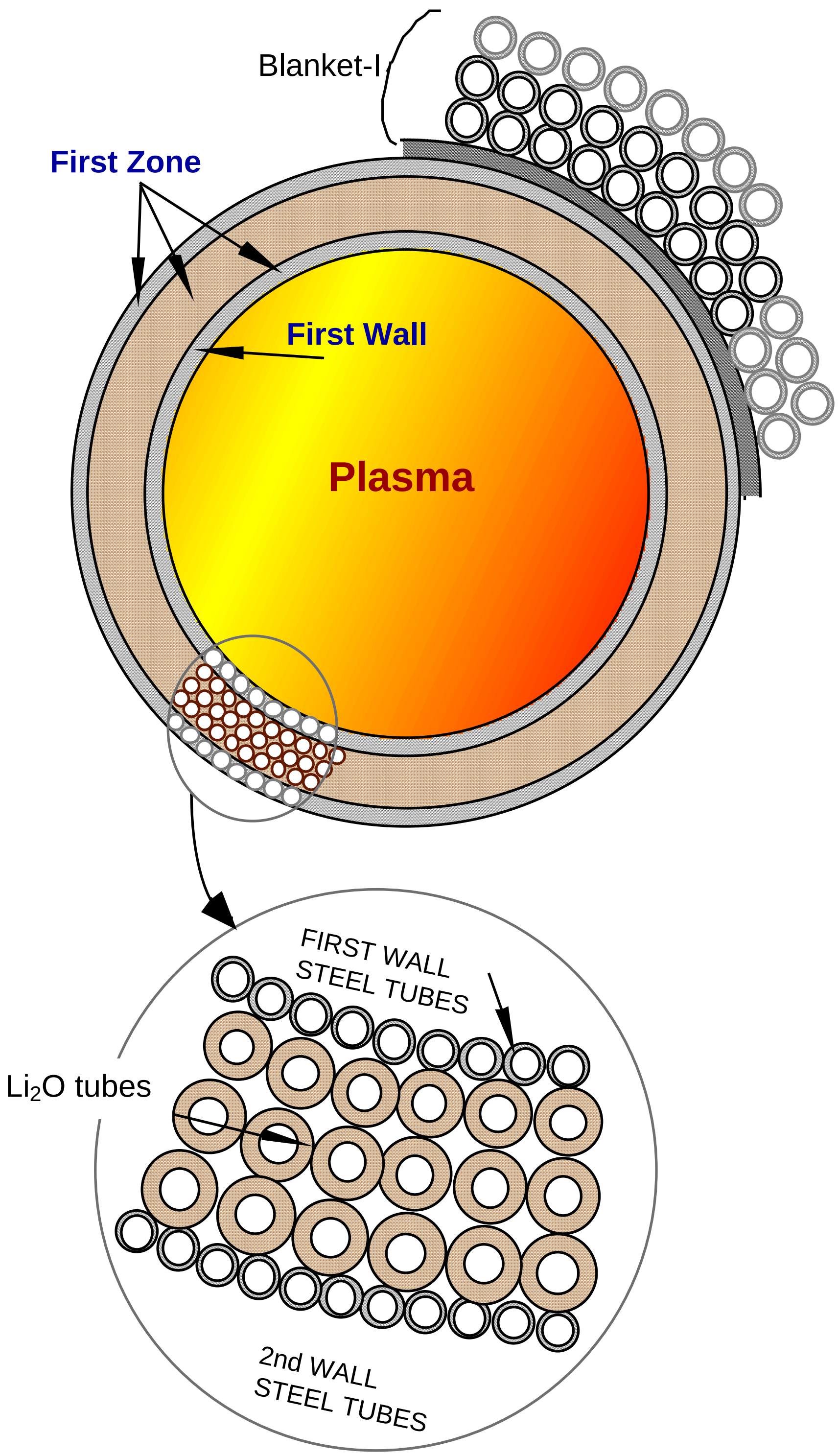

Figure 2-4: Detail of the first zone of the FRC.

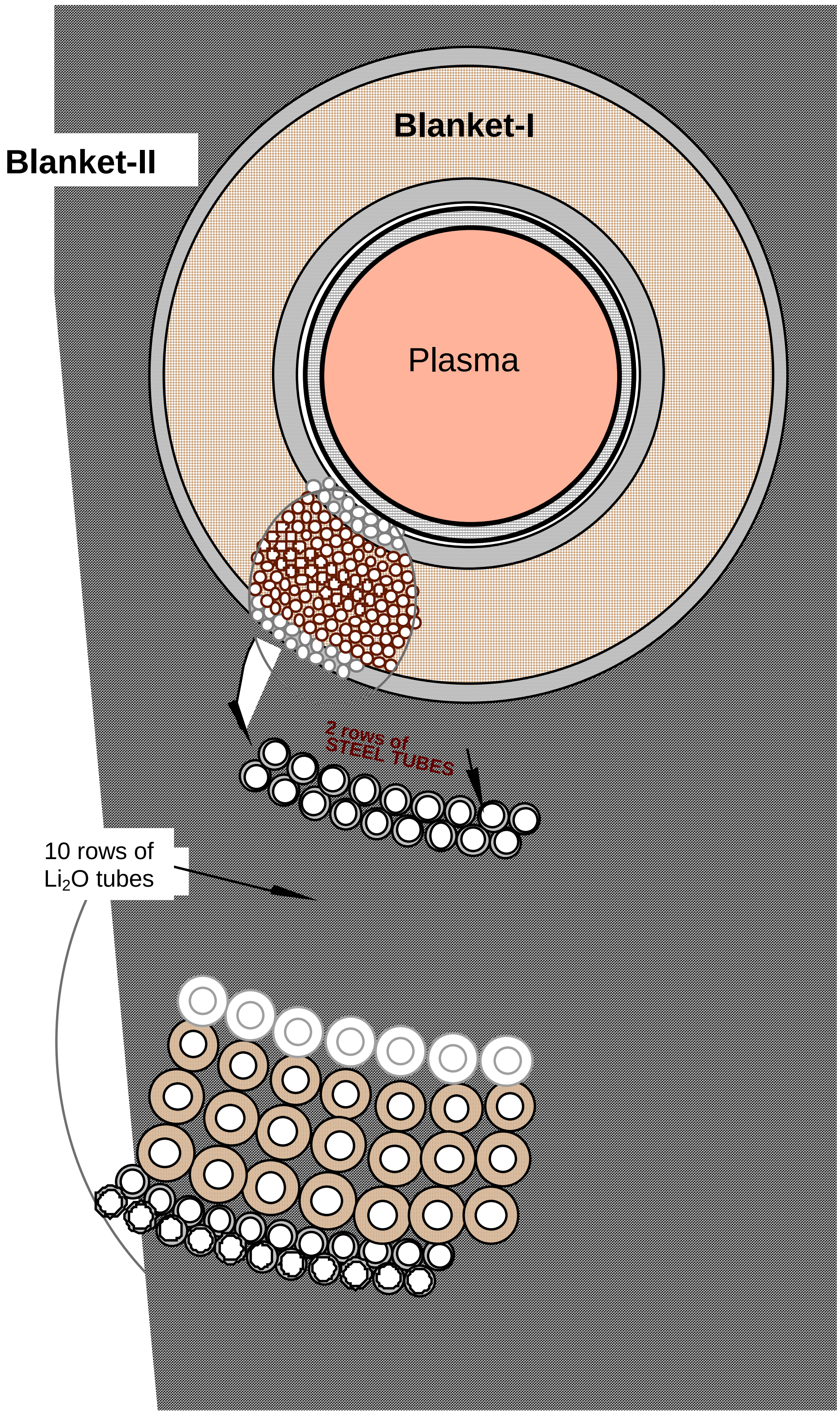

Figure 2-5: Detailed cross section of blanket-I with the plasma in the core of the FRC.

2.3 Coolant routing

To maximize the power conversion thermal efficiency the outlet helium temperature must be at the maximum attainable value. To achieve maximum power conversion thermal efficiency without violating all the constraints on the reactor materials' maximum operating temperature, the helium coolant routing must be optimized. The helium gas coolant path is continuous throughout the entire FRC module. The route of the He gas coolant is as follows:

- Cold He (T = 380°C) first enters all steel walls (first wall, blanket walls, and shield (steel)) to keep their temperature below 650°C.
- Then He gas enters (T = 530°C) the Li_2O zones (first zone, blanket-I, and blanket-II) to remove the generated volumetric heating.
- The hot helium exits the blanket to the heat exchanger at about 830°C. The secondary helium exits the heat exchanger at about 800°C.

Figure 2-6 shows the coolant routing through the FRC coolant channels. The helium mass flow rate would be adjusted to make the He exit at a temperature of 830°C. The Brayton power cycle efficiency is about 52% for the cycle He maximum temperature of 800°C. Figure 2-7 shows the net efficiencies vs. peak temperature for several power cycles: steam, Brayton, and GA/Field cycles.

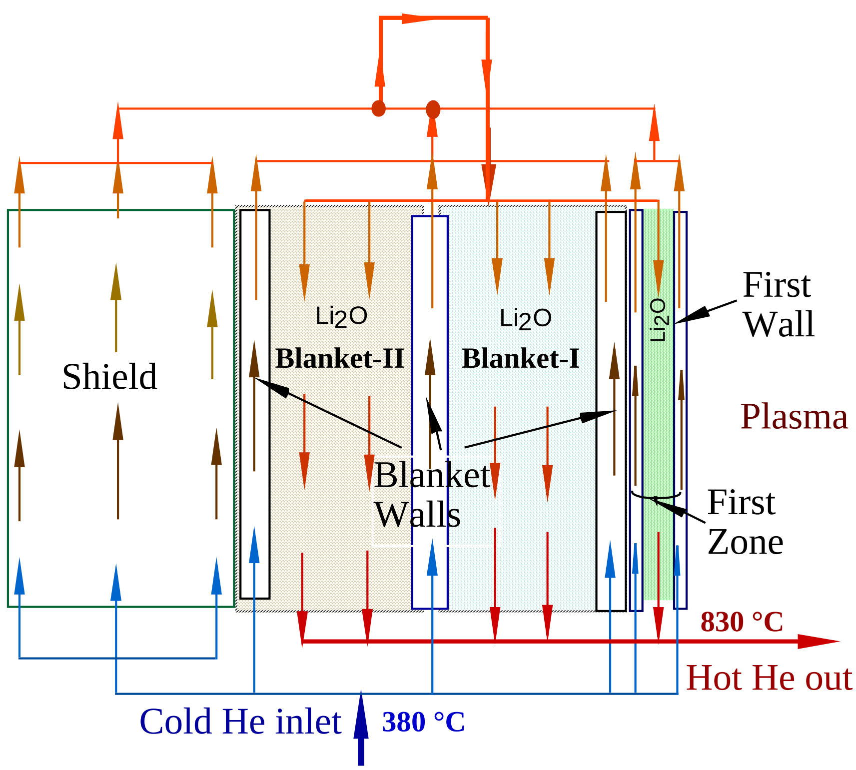

Figure 2-6: Coolant routing in the FRC first wall blanket and shield.

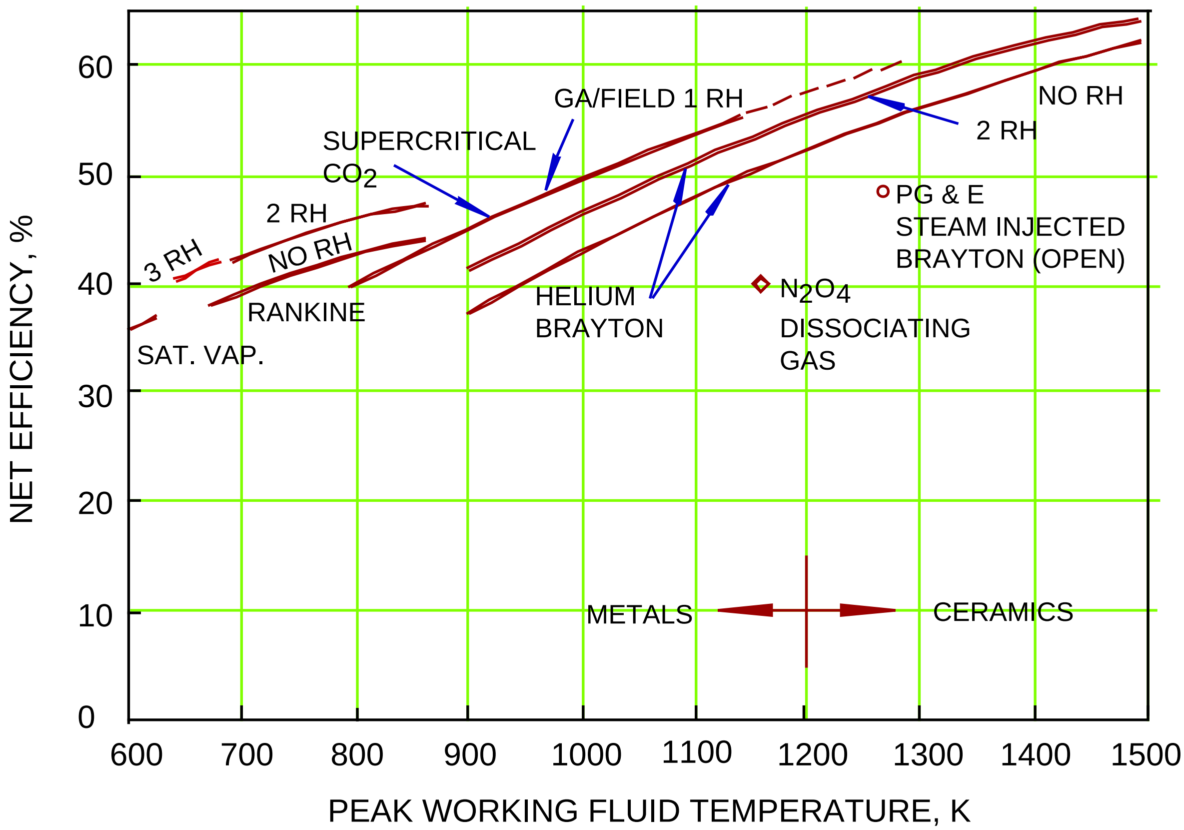

Figure 2-7: Net efficiencies vs. peak temperature for several power cycles: steam, Brayton, and GA/Field cycles (extracted from Ref. 3).

2.4 Thermal hydraulics calculations

The total heating/module (volumetric and surface) in the first wall = 79.6 MW. Assuming that the helium coolant has the following parameters:

- Helium gas flow temperature rise in the first wall is 200°C.
- Gas pressure is 18 MPa.
- Properties of helium gas are calculated at the average temperature of the component it cools.
- Properties of Li_2O are calculated at the average temperature of the component it cools.

Table 2-1 shows a summary of the all the inputs into the thermal response calculations and a brief summary of the general dimensions of the FRC design.

Table 2-1: Main Parameters (Dimensions and the Specific Steady-State Thermal Loads) of the FRC Design.

Modules	
Length (m)	2.50
Number of modules	10
First zone	
First Wall (steel)	
Radius from the center of the plasma (m)	2.0
Outer tube diameter (mm)	15
Thickness of steel tube (mm)	2.5
Surface heating (MW/cm^2)	0.2
Volumetric heating in solid steel (W/cm^3)	38.43
First Li_2O zone	
Number of rows	3
Width (m)	0.1575
Percentage of Li_2O (without steel)	30%
Percentage of He (without steel)	70%
Outer tube diameter (mm)	31.5
Average volumetric heating (Li_2O+He) (W/cm^3)	13.04
Average volumetric heating in solid Li_2O (W/cm^3)	33.12
Second Wall (steel)	
Outer tube diameter (mm)	15
Thickness of steel tube (mm)	2.5
Volumetric heating in solid steel (W/cm^3)	24.88
Blanket-I & Blanket-II	
Percentage of steel	8.3%
Percentage of Li_2O (without steel)	40%
Percentage of He (without steel)	60%
Blanket-I	
Wall-I (steel)	
Number of rows	2
Outer tube diameter (mm)	50
Thickness of steel tube (mm)	14.1
Volumetric heating in solid steel (W/cm^3)	15.8
First Li_2O zone	
Thickness (m)	0.535
Average volumetric heating (Li_2O+He) (W/cm^3)	2.3
Average volumetric heating in solid Li_2O (W/cm^3)	5.75
Wall-II (steel)	
Number of rows	2
Outer tube diameter (mm)	50
Thickness of steel tube (mm)	14.1
Volumetric heating in solid steel (W/cm^3)	1.0

Table 2-1 (cont):

Blanket-II	
First Li_2O zone	
Thickness (m)	0.535
Average volumetric heating (Li_2O+He) (W/cm^3)	0.13
Average volumetric heating in solid Li_2O (W/cm^3)	0.325
Wall-II (steel)	
Number of rows	2
Outer tube diameter (mm)	50
Thickness of steel tube (mm)	14.1
Volumetric heating in solid steel (W/cm^3)	0.07
Shield	
Thickness (m)	0.60
Percentage of steel	90%
Percentage of Li_2O	0%
Percentage of He	10%
Average volumetric heating (W/cm^3)	0.028

2.5 Results of thermal hydraulics calculations of the FRC components

The total nuclear heating and surface heating (per module) in the steel is 60 MW. The total nuclear heating (per module) in the Li_2O is 120 MW. The helium coolant enters the steel tubes at a temperature of 380°C and exits the steel tubes at a temperature of 530°C. The heat balance requires that the helium mass flow rate be 76.5 kg/s for a 150°C He gas temperature rise. The helium coolant enters the Li_2O tubes after it exits the steel tubes at a temperature of 530°C and exits the Li_2O tubes at a temperature of 830°C. The thermal heat load in the steel tubes is half the thermal heat load in the Li_2O tubes. Using the same helium mass flow rate of 76.5 kg/s inside and outside of the Li_2O tubes would result in a He gas temperature rise of 300°C. Figure 2-8 shows a sketch of these results with the coolant routing.

Table 2-2 shows the properties of helium coolant used in the thermal hydraulics calculations at average temperatures of 455°C and 680°C. The properties of Li_2O are reported at an average temperature of 800°C. The average helium velocity in each tube of steel and Li_2O is calculated. Table 2-3 shows the total steady state heat load, helium gas mass flow rate, and the helium gas average velocity for each component of one module.

Table 2-2: Physical Properties of Helium and Li_2O Used in the Thermal Analysis.

Material	He (455°C)	He (680°C)	Li_2O
Thermal conductivity (W/mK)	0.282	0.34	3.74
Specific heat (J/kg K)	5.19×10^3	5.19×10^3	2.878×10^3
Viscosity (Ns/m^2)	3.65×10^{-5}	4.35×10^{-5}	N/A
Pr	0.67	0.67	N/A

Table 2-3: The Steady-State Thermal Load per Module, Helium Coolant Mass Flow, and Helium Coolant Average Velocity in Different Components of the FRC Design.

Zone	*Total heating (MW)*	*Helium mass flow rate (kg/s)*	*Helium velocity (m/s)*
First zone			
First wall (steel)	15.7	20.17	26.4
First Li_2O zone	67.55	48.38	3.44
Second wall (steel)	6.14	7.89	9.22
Blanket-I			
Wall-I (steel tubes)	34.7	44.57	18.06
Li_2O	48.76	31.32	0.68
Wall-II (steel tubes)	2.2	2.82	1.14
Blanket-II			
Li_2O	3.41	2.19	0.039
Wall-III (steel)	0.15	0.2	0.078
Shield			
Bulk (steel)	0.64	0.83	0.0046
Total	**180**	**76.5**	

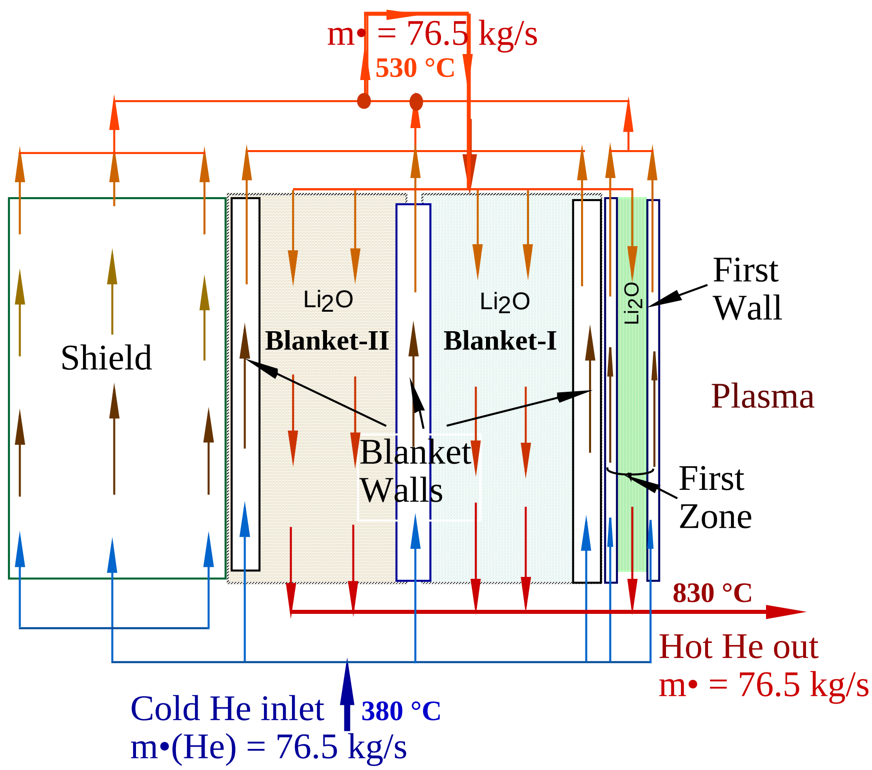

Figure 2-8: Helium coolant routing and the corresponding helium coolant mass flow rate and temperature at inlet and exit of FRC components.

The coolant pressure drop is strongly dependent on the tube size and gas velocity. This limits the lower value of the Li_2O tube radius (the smaller the size and void fraction of the Li_2O tubes the larger the pressure drop). On the other hand the recommended maximum operating temperature of the Li_2O is about 1000°C to avoid sintering, and this limits the maximum radius of the Li_2O tubes. Figure 2-9 shows the variation of heat transfer coefficient with temperature for different first zone components. In Figure 2-10 the heat transfer coefficient of He in the Li_2O tubes of the first zone is presented in detail.

Thermal hydraulics analysis is performed using a finite element code (ANSYS 5.5) to study the effect of the steel tube dimensions on the temperature distribution and the maximum value in the steel tube wall. Figures 2-11, 2-12, and 2-13 illustrate the temperature distribution in the first wall steel tube at three different positions. The maximum temperature is at the exit and is 635°C.

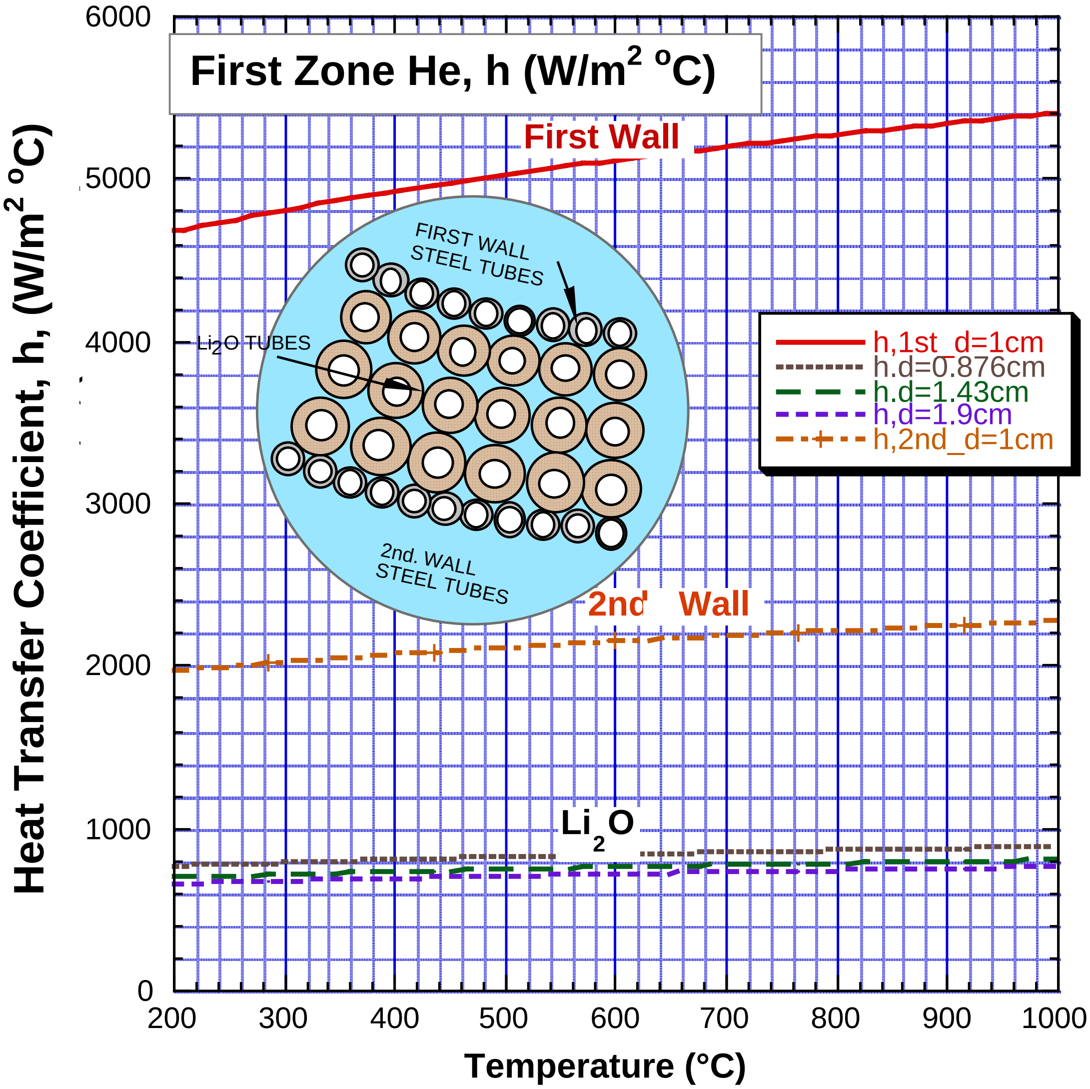

Figure 2-9: Heat transfer coefficient of coolant helium in the first zone (First wall, first zone Li_2O tubes, and second wall).

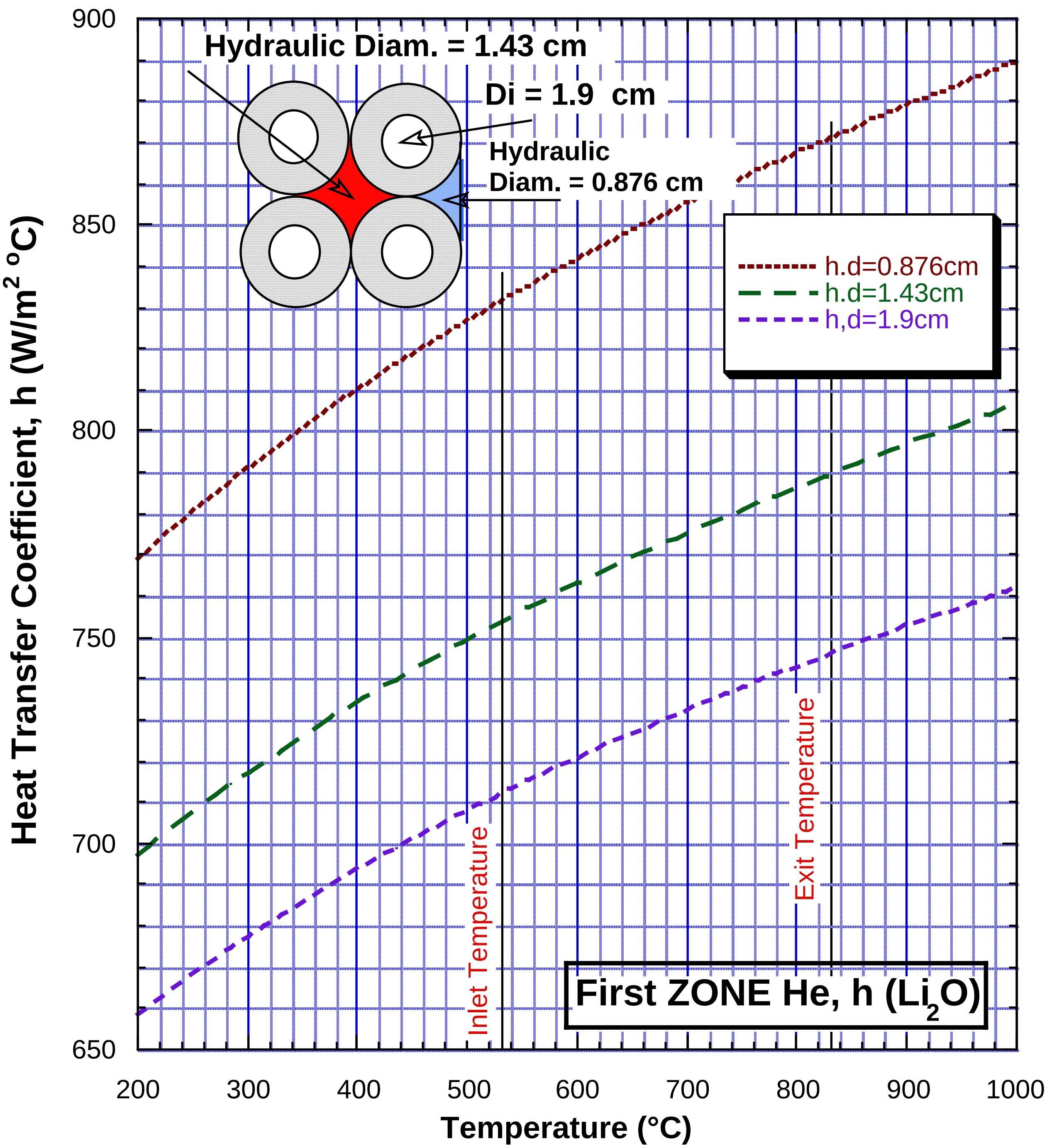

Figure 2-10: Heat transfer coefficient of coolant helium in the first zone Li_2O tubes.

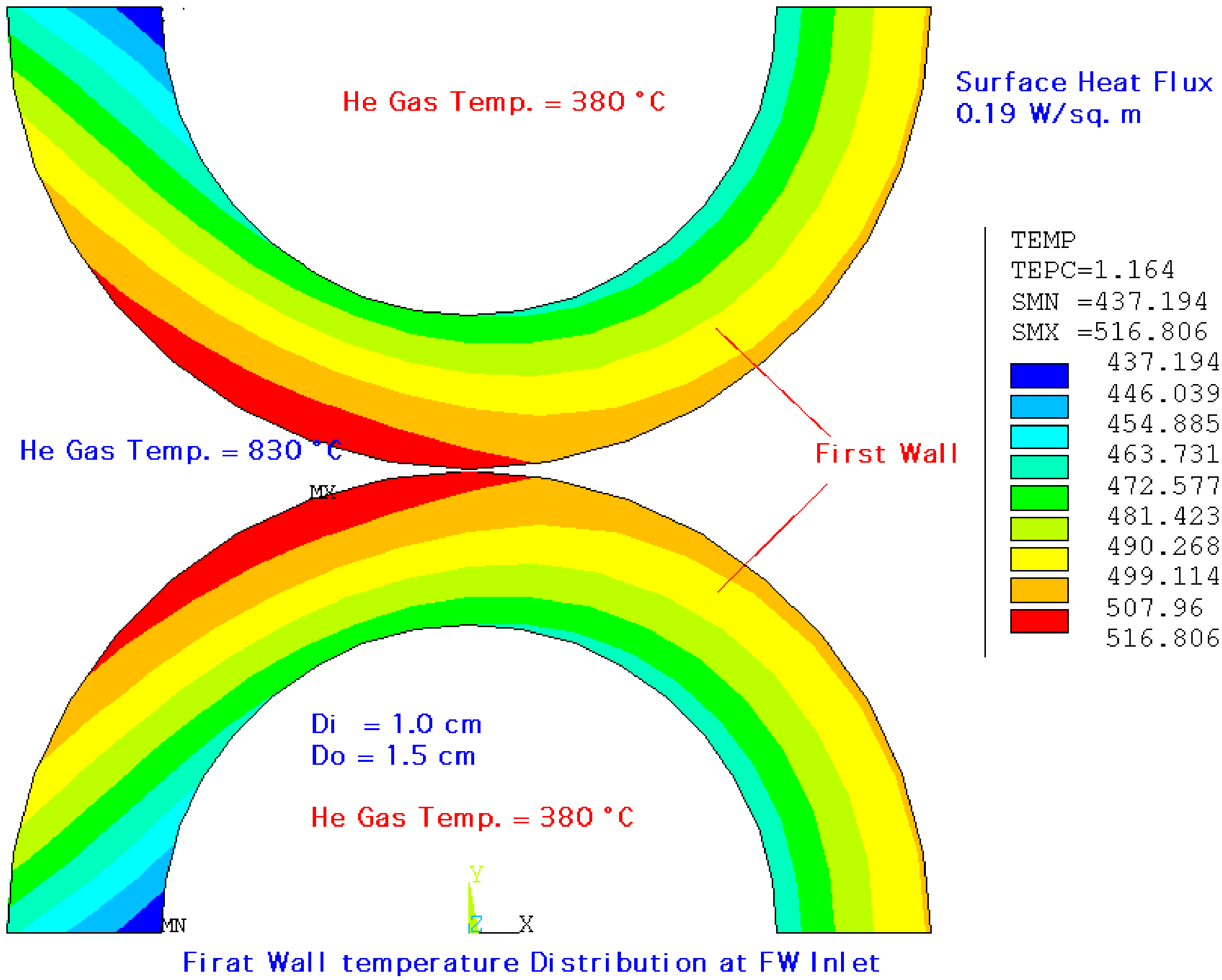

Figure 2-11: Temperature distribution at the inlet of the first wall.

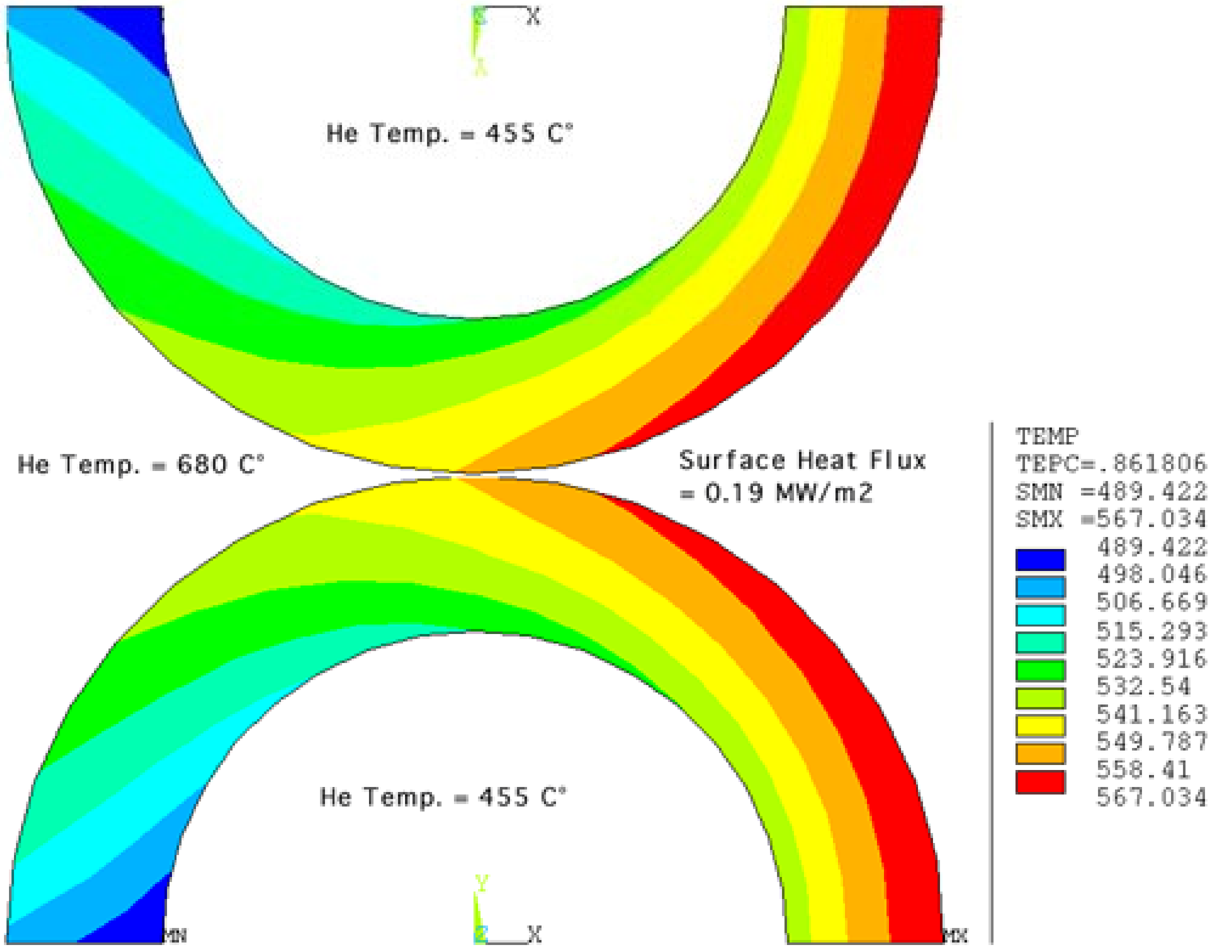

FW Temperature Distribution at mid-distance

Figure 2-12: Temperature distribution at the mid-point of the inlet and the outlet of the first wall.

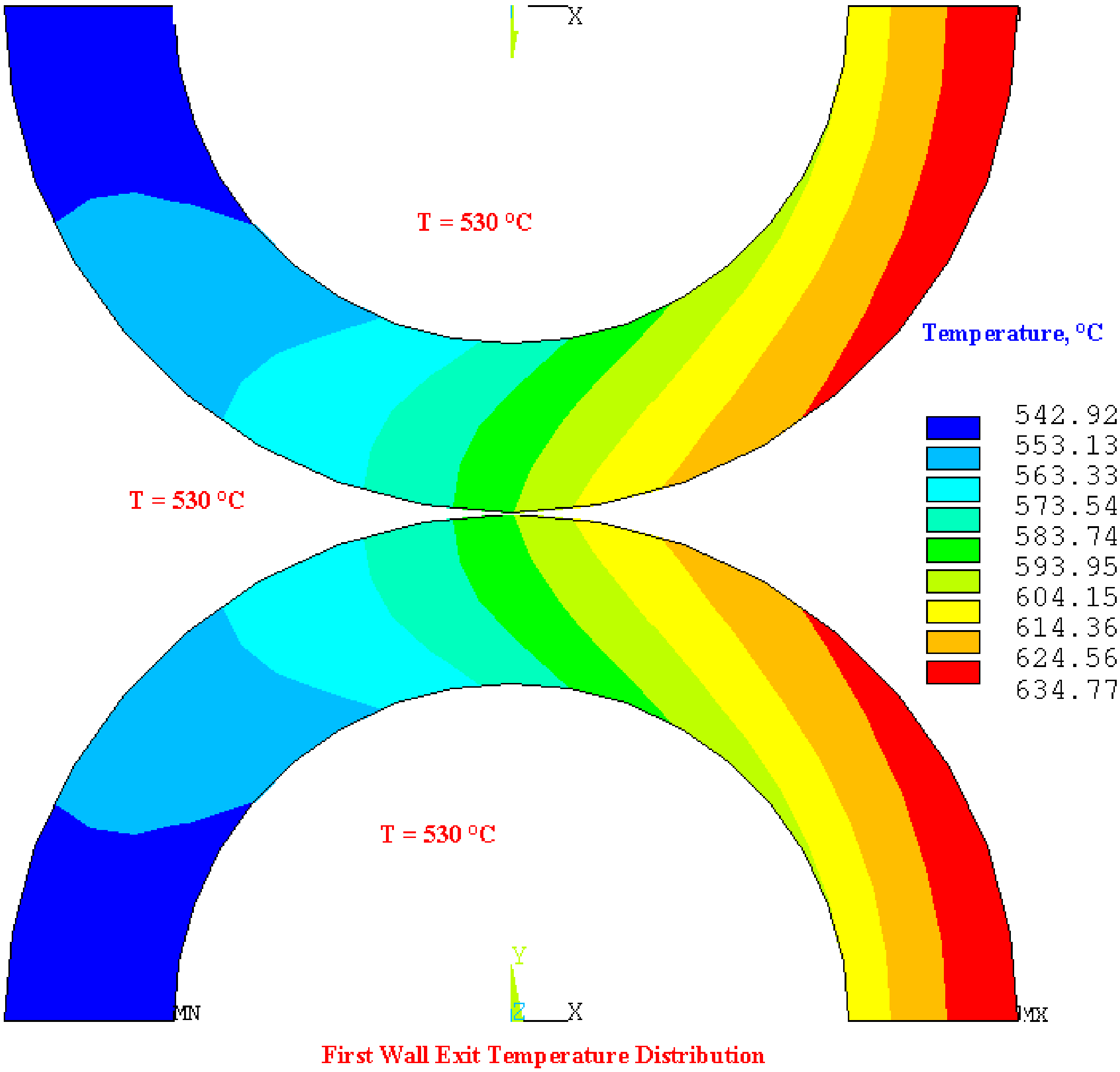

Figure 2-13: Temperature distribution at the exit of the first wall.

2.6 Limits on the Li_2O tube dimensions

Thermal hydraulics analysis is performed to study the effect of the Li_2O tube dimensions on the temperature difference between the maximum value at the Li_2O tube wall and the free stream helium temperatures. The maximum temperature of Li_2O would occur at the helium exit at the first zone. Figure 2-14 shows a maximum temperature of 1003°C for the nearest Li_2O tube to the first wall.

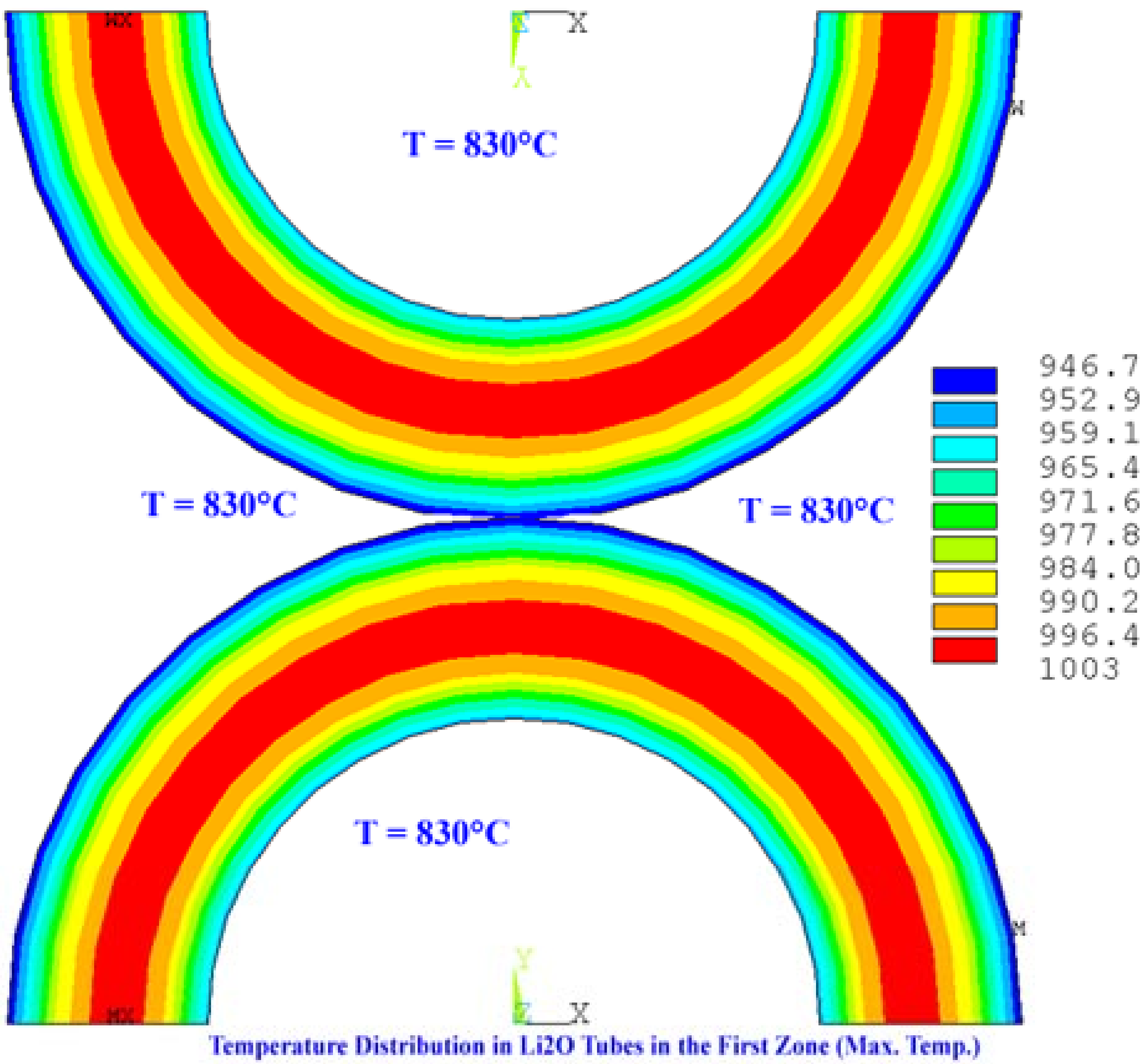

Figure 2-14: Temperature distribution at the exit of the first zone Li_2O tube.

2.7 Maintenance

The special geometry (cylindrical) facilitates reasonable, practical, maintenance schemes that minimize the downtime and cost. The modular design allows the movement of the individual modules in the axial direction. To keep the vacuum integrity inside the reactor during operation a pillow type of overlap is used between modules. To maintain a given module, the pillow at the two interfaces is broken, all the pipes are disconnected, and the rest of the modules are slid away on both sides far enough to disengage from the module under consideration. This module is moved to a hot cell, where it could be maintained and replaced with another standby module. Figure 2-15 describes this scheme.

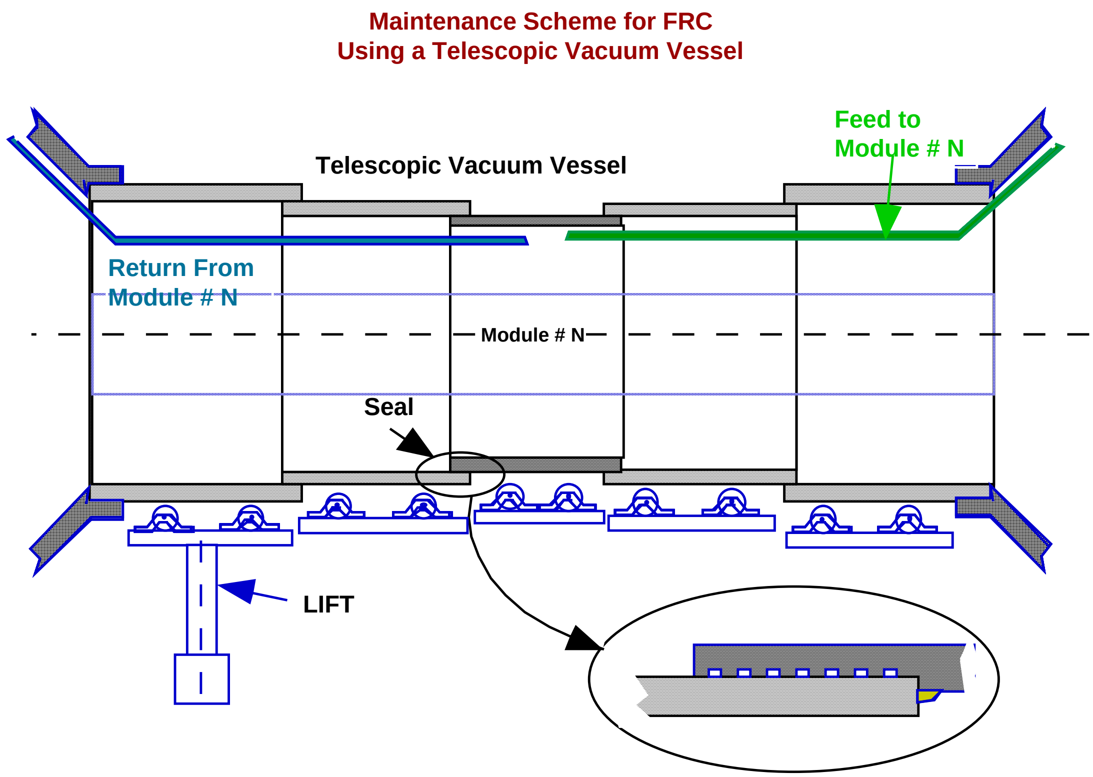

Figure 2-15: Maintenance scheme for D-T FRC Scoping Study Fusion Core.

2.8 References for Section 2

1. Steven J. Zinkle, ORNL, *VLT News* **1**, #5 (Virtual Laboratory for Technology Newsletter, UCSD, Oct. 1999).

2. R. L. Klueh, N. Hasimoto, R. F. Buck, and M. A. Sokolov, "A Potential New Ferritic/Martensitic Steel for Fusion Applications," *Journal of Nuclear Mat*erials (to be published).

3. Robert F. Bourque, "Power Conversion System," Comments presented at ARIES reactor design meeting (University of Wisconsin, Nov. 7-8, 1990).

4. S. Ergun, "Fluid Flow through Packed Column," *Chemical Engineering Progr*ess **48**, #2, 89 (1952). A. Bejan, *Convection Heat Transfer,* Chapter 12 (Wiley, New York, 1995).

3 WISC: the WIsconsin Systems Code

3.1 Introduction

The WIsconsin Systems Code, WISC, is a C code for calculating field-reversed configuration (FRC) and tokamak power plant physics and engineering. An input file provides the data necessary for the code to calculate global power balance to determine the injection power necessary to sustain the plasma. The electron power balance is solved to obtain a self-consistent electron temperature. The power losses are due to charged particle transport, neutrons, and bremsstrahlung radiation. The code provides three energy conversion processes: direct conversion to electricity, thermal conversion, and conversion by both methods simultaneously.

The code accounts for six ion species: protons, deuterium (D), tritium (T), ^{3}He, ^{4}He, and an impurity. It determines the density of these species as a fraction of the deuterium density. The density of deuterium is based on either the β (plasma pressure/magnetic field pressure) limit or an input fixed averaged fuel density. The total ion pressure includes a contribution from a slowing-down distribution of fusion products.

WISC provides several search options. In these, the code changes a parameter(s) so that the net electrical power converges to a desirable value, usually 1000 MW_e. The FRC version has additional options, to converge to: a desired neutron wall load, the rotating magnetic field (RMF) current-drive power, or a specified injection power. During a run the user may change the values of the input variables. Calculated results are displayed on the screen and may be saved to an output file if desired.

The WISC code is a modification of RAGE3 (Reactor Analysis by Gil Emmert). RAGE3 had tokamak physics exclusively, which has been minimally changed in the WISC version. The option of whether to run the tokamak version or the FRC version is set by using preprocessor macros (changing the #ifdef statement in the device.h file). The code must be recompiled each time the #ifdef statement is reset.

Below we describe the physics and engineering models contained in WISC. Our focus is on the FRC physics; the tokamak version is similar. The units in the code are SI except for temperature and energy, which are in keV.

3.2 Nomenclature

This section contains a list of variables used in formulas, plus their names in the computer code, units, and definitions.

3.2.1 Subscripts

The subscript i on some of the variables represents a label for an ion species. The subscripts are the same for background ions as well as the fast ions. The identifications are as follows:

#	Ion Species
1	proton
2	deuterium
3	helium-3
4	alpha
5	tritium
6	impurity

3.2.2 Variables

Symbol	Name in code	Units	Definition
β	beta		ratio of plasma pressure to magnetic pressure
β_B	avbeta		Barnes beta
Δ_b	delb	m	blanket radial thickness
Δ_c	delc	m	coil cryostat radial thickness
Δ_{edge}	deledge	m	edge-layer radial thickness
Δ_m	delm	m	coil radial thickness
Δ_s	dels	m	shield radial thickness
Δ_{tot}	deltot	m	total radial thickness (first wall to coil outer edge)
ε_0		$F\ m^{-1}$	vacuum permittivity
η		ohm m	first-wall resistivity
η_{eff}	cureff		current drive efficiency
η_{dir}	etadir		direct conversion efficiency
η_{therm}	etatherm		thermal conversion efficiency
γ_{eprof}			electron temperature profile factor
γ_{iprof}			ion temperature profile factor
γ_w	reflect		first-wall reflectivity
κ	var_kap		radial profile parameter in FRC profiles

κ_{frc}	kappa_FRC		FRC elongation
λ_B		m	De Broglie wavelength
λ_D		m	Debye length
Λ_e	ce		electron Coulomb logarithm
Λ_i	cr		ion Coulomb logarithm
μ		amu	normalized ion mass
$\overline{\mu}$	mbar	amu	average ion mass
μ_0		H m^{-1}	$4\pi\left(10^{-7}\right)Hm^{-1}$
ρ_{i0}		m	external-field ion gyroradius
σ	var_sig		radial structure parameter in FRC profiles
τ_E	taue	s	energy confinement time
τ_p	taup	s	particle confinement time
τ_s	tslow	s	fast ion slowing down time
A_c	apcoil	m^2	coil cross-sectional area
A_w	awall	m^2	area of first wall
B_c	bc	T	external magnetic field
e		C	electron charge
E_c	ec	keV	critical energy for fast ion slowing down
E_i	e[i]	keV	energy of ion species i (fusion product)
E_0	e[i]	keV	birth energy of fast ion
E_{tail}	ttail	keV	energy of the enhanced deuteron tail
f_{elect}			fraction of fast ion energy to background electrons
f_h	fhole		fraction of the wall for waveguides
f_i	impconc		impurity concentration fraction of the ion density
f_{inj}	finj		fraction of the injection power going into the ions
f_{ion}			fraction of a fast ion energy going into background ions
h		J s	Planck's constant
h_{mag}	htgmag	MW/m	nuclear heating of the magnet per unit length
I_c	eyep	A	total coil current
$\overline{j}$	djbar	A/m^2	coil average current density
$\overline{j}_{\max}$	djbarm	A/m^2	maximum allowed coil average current density
k_{therm}	ktherma		option for energy conversion process
L_s	length	m	length of separatrix
M_{dd}	mddn		D-D neutron energy mult factor for blanket/shield
M_{dt}	mdtn		D-T neutron energy mult factor for blanket/shield
M_b	wblkt	m^3	blanket mass
M_m	wcoil	m^3	magnet mass
M_s	wshld	m^3	shield mass
M_{strt}	wstrt	m^3	support structure mass

m_e		kg	electron mass
m_i	amu[i]	amu	mass of ion species i
n_τ	nuwtaus		wave drag coefficient/tauslow
n_e	denel	10^{20} m^{-3}	electron density
$\langle n_e \rangle$	avdene	10^{20} m^{-3}	average electron density
n_{fix}	denfix	10^{20} m^{-3}	average fuel ion density
n_i	den[i]	10^{20} m^{-3}	density of ion species i
$\langle n_i \rangle$	avdeni	10^{20} m^{-3}	average ion density
n_0	den[0]	10^{20} m^{-3}	total ion density
n_{prof}			density profile
n_{tail}	dentail		density of the fast deuteron tail
p_{allow}	press	keV/m^3	allowed plasma pressure
p_{brems}	pbrems	MW	bremsstrahlung power
p_{cryo}	pcryo	MW	cryoplant power
p_{elect}	pfusel	MW	fusion power going to electrons
p_{enet}	pelect	MW	net electrical power
p_{fast}	avpfast	keV/m^3	fast ion pressure
p_{gross}	pegross	MW	gross electric power
p_{house}	housepower	MW	housekeeping power
p_{ie}		MW	electron-ion rethermalization power transfer
p_{inj}	pinj	MW	injected power
p_n^{dd}	pneutdd	MW	neutron power from D-D reactions
p_n^{dt}	pneutdt	MW	neutron power from D-T reactions
p_{nuc}	pnuc	MW	magnetic heating power
p_{pump}	pumpower	MW	pumping power
p_{recirc}	precirc	MW	recirculating power
p_{rmf}	RMFpow	MW	rotating magnetic field power
p_{syn}	psynch	MW	synchrotron power
p_{th}	pthermal	MW	thermal power
p_{tot}	pfustot	MW	total charged-particle fusion power
p_q	ptrans	MW	transport power
p^e_{trans}		MW	electron transport power
p_{wall}	walload	MW	neutron walload
Q_r			energy per fusion reaction (charged particle)
r_c	rc	m	conducting wall inner radius
r_s	rs	m	separatrix radius
r_w	rw	m	first wall radius
R_{tau}	tauratio		ratio of particle to energy confinement time

R_{hel}	helratio		ratio of helium-3 to deuterium
R_i	ratio[i]		ratio of ion species i density to deuterium density
$R_{i\sigma v}$		$m^3\ s^{-1}$	fusion reaction rate for reaction i
$\langle\sigma v\rangle_i$	sigv[i]	$m^3\ s^{-1}$	average reaction rate for reaction type i
R_0		m	O-point radius
R_{trit}	tritratio		ratio of tritium to deuterium
R_{trans}	transratio		ratio of ion to electron energy confinement
R_{tail}		$m^3\ s^{-1}$	fast tail fusion reaction rate
T_e	te	keV	electron temperature
T_i	ti	keV	ion temperature
$U(u)$	cap_u		FRC radial structure function
U_{inj}	uauxhfw	$/We	unit cost of injected power
U_b	ublkt	m^3	blanket unit cost
U_m	ucoil	m^3	magnet unit cost
U_s	ushld	m^3	shield unit cost
U_{strt}	ustrt	m^3	support structure unit cost
v_c		$m\ s^{-1}$	speed of a fast ion at the critical energy
v_0		$m\ s^{-1}$	speed of a fast ion at birth
V_b	vblkt	m^3	blanket volume
$V_{chamber}$	vchamber	m^3	chamber volume
V_m	vpcoil	m^3	magnet volume
V_s	vshld	m^3	shield volume
V_{strt}	vstrt	m^3	total volume of support structure for all systems
V_{tot}	vtot	m^3	total volume to outside of magnets
V_0	vol	m^3	plasma volume
V'/V	vprime[i]		dimensionless volume element at flux surface *i*
x_c			v_0/v_c
x_s	sepratio		ratio of separatrix to conducting wall radius
x_w	wallrat		ratio of conducting wall to first wall radius
z_{crit}	zcrit		control constant for specified accuracy
Z_{eff}	zeff		effective charge
Z_{2eff}	z2eff		density-weighted charge squared
Z_i	z[i]		charge of ion species i
Z_s	ze		slowing down charge

3.3 Description of the WISC code

3.3.1 Initialization

After the user has entered the desired input, the code initializes quantities that never change and sets up the ion species. The code also makes initial guesses for various parameters that need an initial value. These initial guesses will be changed during the calculations. The initialization is performed in the routine initial().

An ion species is assigned a number, which is also an array element index. For example, the mass of deuterium, whose index is 2, is amu[2], and likewise den[2] is its density. The identification of ion species appears in Table 3-1. Note that the charge and relative concentration of the impurity species is an input parameter, and its mass is assumed to be twice its charge.

The code includes four reactions: ^{3}He(d,p)^{4}He, D(d,n)^{3}He, D(d,p)T, and T(d,n,)^{4}He. The identification index of the reactions is shown in Table 3-2. The energies of charged fusion products are constant, and their identification is shown in Table 3-3.

Quantities requiring initial values are shown in Table 3-4. The density of ^{3}He, tritium, and impurities are $n_3 = R_3 n_2$, $n_5 = R_5 n_2$, $n_6 = (n_2 + n_3 + n_5) f_i$ respectively. The electron density, total ion density, and average ion mass are given by

$$n_e = \sum_{i=1}^{6} Z_i n_i \tag{1}$$

$$n_0 = \sum_{i=1}^{6} n_i \tag{2}$$

$$\bar{\mu} = \frac{\sum_{i=1}^{6} m_i n_i}{\sum_{i=1}^{6} n_i} \tag{3}$$

Table 3-1: Index, Mass, and Charge of Plasma Species.

Species or array element number	Ion species	Mass, amu	Charge, z
1	proton	1	1
2	deuterium	2	1
3	helium-3	3	2
4	alpha	4	2
5	tritium	5	1
6	impurity	$2 \times z[6]$	input

Table 3-2: Fusion Reactions Included.

Reaction identification	Fusion reactions
1	$^3He(d,p)^4He$
2	$D(d,n)^3He$
3	$D(d,p)T$
4	$T(d,n)^4He$

Table 3-3: Charged Fusion Products and Their Energies.

Array element number	Associated product	Energy (keV), e[i]
1	proton from $^3He(d,p)^4He$	14680
2	alpha from $^3He(d,p)^4He$	3670
3	^3He from $D(d,n)^3He$	820
4	proton from $D(d,p)T$	3020
5	triton from $D(d,p)T$	1010
6	alpha from $T(d,n)^4He$	3520

Table 3-4: Typical Initial Guesses for Parameters.

Parameter	Typical initial guess
τ_e	10.0
τ_p	10.0
n_1 (protons)	0.0
n_4 (alphas)	0.0
γ_w	$1.0 - f_h$

3.3.2 Charge

Some formulas, such as that for bremsstrahlung radiation, require an *effective* charge. The effective charge is related to the density, which changes, and therefore is calculated whenever needed. The effective charge is calculated in the routine zeffect(). The effective charge may be written as

$$Z_{eff} = \frac{\sum_{i=1}^{6} n_i Z_i^2}{\sum_{i=1}^{6} n_i Z_i} \tag{4}$$

Two other charge-related quantities required are Z_{2eff} and Z_s. The routine z2effect() calculates the number:

$$Z_{2eff} = \frac{\sum_{i=1}^{6} n_i Z_i^{\ 3}}{\sum_{i=1}^{6} n_i Z_i} \tag{5}$$

Z_s is related to the slowing down of the fast ions. Fast ions in the plasma interact with background ions and electrons through Coulomb collisions. The process causes the fast ions to slow down, lose their energy, and heat the background plasma. The number Z_s is the effective energy transfer charge for this slowing down and rethermalization process. The routine zslow() calculates Z_s for a multi-species plasma. The formula for Z_s is

$$Z_s = \sum_{i=1}^{6} \frac{n_i Z_i^{\ 2}}{n_e m_i} \tag{6}$$

3.3.3 Coulomb logarithm

The Coulomb logarithm (or Coulomb log) accounts for the cumulative small angle scattering and the rare large angle deflection in Coulomb collisions. The Coulomb log is the natural log of the ratio between the maximum collision impact parameter and the minimum collision impact parameter. The maximum impact parameter is generally taken to be the Debye length because, due to Debye shielding, the Coulomb force is negligible beyond the Debye length. The minimum impact parameter can be either of two scale lengths. One of these is the de Broglie wavelength accounting for quantum mechanical effects. The other accounts for large angle scattering occurring when the potential interaction energy is comparable to the kinetic energy of the charged particle. The minimum impact parameter is the larger of the de Broglie wavelength and the large-angle scattering length. Two Coulomb logarithms that are calculated in the code are the electron Coulomb log and the ion Coulomb log between fast ions and background ions.

The electron-ion Coulomb log, which is the same for ion-electron interactions, is calculated in the elcoul() routine. There are several expressions for the electron Coulomb log depending on the electron temperature, the ion temperature, the mass of the ion, and the charge of the ion. The relevant electron Coulomb log expression in our units is

$$\Lambda_e = 14.8 - \ln\left(n_e^{1/2} T_e^{-1}\right) \tag{7}$$

For fast ions such as 3.5 MeV alphas and 14.7 MeV protons the de Broglie wavelength is more applicable. This might not be true when the fast ion has slowed down to thermal energy. We will use the de Broglie wavelength since the initial slowing down time plays a role in determining the fast ion pressure. We can obtain the ion Coulomb log by combining three equations, the Debye length, the de Broglie wavelength, and the energy of the fast ion.

$$\lambda_D = \sqrt{\frac{\varepsilon_0 T_e}{2 n_e e^2}} \tag{8}$$

$$\lambda_B = \frac{h}{v\mu} \tag{9}$$

$$E_i = \frac{m_i v^2}{2} \tag{10}$$

where v is the speed of the fast ion and m_i is its mass. Combining the equations gives us the ion Coulomb log as

$$\Lambda_i = \ln\left[\mu\sqrt{\frac{\varepsilon_0 T_e E_i}{n_e e^2 h^2 m_i}}\right] \tag{11}$$

We can use the average ion mass in the reduced mass. Plugging in constants, we obtain the ion Coulomb log as

$$\Lambda_i = 17.1 + \ln\left[\frac{m_i\overline{\mu}}{m_i + \overline{\mu}}\sqrt{\frac{E_i T_e}{n_e m_i}}\right] \tag{12}$$

The ion Coulomb log is calculated in the routine ioncoul().

3.3.4 Geometric and density parameters

The params() routine calculates various geometric and density parameters that vary with each case, but not within an iteration for the electron temperature or density. This routine is also where the array for profiles is set up for doing integration. Formulas for the geometric quantities are shown in Table 3-5.

The FRC profiles used are not true equilibria but are quasi-equilibria and an extension of the rigid rotor. The equilibria are assumed to be elongated so that pressure balance holds in the form

$$p + \left(\frac{B^2}{2\mu_0}\right) = \left(\frac{B_c^2}{2\mu_0}\right) = const \tag{13}$$

The resulting profiles follow:

Magnetic field: $$B(r,z) = B_c \tanh U \qquad \left(B_r \approx 0,\ \ B \approx B_z\right) \tag{14}$$

Current density: $$j_\theta(r,z) = \frac{B_c^2}{2\mu_0}\frac{2r}{R^2(z)}U^{/}\sec h^2 U \tag{15}$$

Pressure: $$p(r,z) = p_m \sec h^2 U \qquad \left(p_m = \frac{B_c^2}{2\mu_0}\right) \tag{16}$$

Density: $$n(r,z) = n_m\left(\frac{p}{p_m}\right)^{1/\gamma} = n_m\left(\sec h\ U\right)^{2/\gamma} \tag{17}$$

Temperature: $$T(r,z) = T_m\left(\frac{p}{p_m}\right)^{(\gamma-1)/\gamma} = T_m\left(\sec h\ U\right)^{2(\gamma-1)/\gamma} \tag{18}$$

The adiabatic index γ is the ratio of the heat capacity at constant pressure to the heat capacity at constant volume, taken to be 4/3. The electron and ion temperatures may have different peak value but are assumed to have the same profile. The functions $R = R(z)$ and $U = U(u)$ give the axial structure and the radial structure respectively. More explicitly we have

$$U(u) = \kappa \frac{\tanh^{-1} \sigma u}{\sigma} = \frac{\kappa}{2\sigma} \ln\left(\frac{1+\sigma u}{1-\sigma u}\right) \tag{19}$$

$$U' = dU/du = \kappa/\left(1 - \sigma^2 u^2\right) \tag{20}$$

$$u = r^2/R^2(z) - 1 \tag{21}$$

$$R(z) = R_0 \left(1 - z^4/\left(L_s/2\right)^4\right)^{1/2} \tag{22}$$

Here *u* is the conventional minor radius variable, R_0 is the radius where $B_z = 0$. The O-point radius, R_0, is related to the separatrix radius through the relation $r_s = R_0\sqrt{2}$. Two parameters, κ and σ, specify the radial structure. The rigid rotor case is recovered in the limit $\sigma \to 0$.

These profiles are in terms of (*r*,*z*). For volume averaging we need to integrate over the volume. Fortunately we can reduce the multiple integral over the various variables into a single variable integration. We do this by converting the volume integral into an integral over the minor radius variable *u*. We now show one way of converting the multiple integral to the single integral.

Consider a small volume element, $dV = \pi r^2 dz$, and since *r* is a function of *u* and *z*, we can integrate over z to get the volume in terms of *u*. Writing this out explicitly we get

$$\begin{aligned} V(u) &= \int_{-L_s/2}^{L_s/2} R_0^2 \left(1 - \frac{z^4}{\left(L_s/2\right)^4}\right)(u+1)\,dz \\ &= \frac{8\pi R_0^2 L_s}{10}(u+1) = 2\pi r_s^2 L_s\,(u+1) \end{aligned} \tag{23}$$

where $\frac{dV}{du} = \frac{8\pi R_0^2 L_s}{10} = 2\pi r_s^2 L_s$.

For any function $f(r,z) = f(u)$ we can integrate over *u* as

$$\int f(r,z)dV = \int f(u)\frac{dV}{du}du \tag{24}$$

The limit on the minor radius variable is $-1 \le u \le 1$. At the $z = 0$ plane, $u = 0$ corresponds to the O-point radius, $u = -1$ corresponds to the z-axis, and $u = 1$ is the separatrix radius.

For profiles such as the current density we need to integrate over an area. We can perform an analogous procedure to the volume for the change of variable. That is, for a small area element, $dA = 2rdz$ gives

$$A(u) \approx 2\left(\frac{1.748 R_0 L_s}{2}\right)\sqrt{u+1} \tag{25}$$

The profiles are too complicated to perform analytically and, as a result, numerical approximations are a necessity. This routine sets up the value of the profile at a specified point. Each point is an element of an array. In the code we work with dimensionless volume so that dV/du or V' is actually divided by the FRC volume, which is represented in the code by vprime[i]. The integral is approximated using Simpson's rule. Quantities appearing inside the integral below have profiles in them while those outside the integral are constants.

The routine params() also returns the allowed plasma pressure. The allowed plasma pressure for the FRC is currently set to be the product of the external magnetic pressure with the Barnes beta, $1-\frac{x_s^2}{2}$.

Table 3-5: Various Geometric Quantities.

Symbol	**Formulas**	**Geometric quantity**
r_c	$x_w r_w$	conducting wall radius
r_s	$x_s r_c$	separatrix radius
β_B	$1-\frac{x_s^2}{2}$	Barnes beta
κ_{frc}	$\frac{\left(L_s/2\right)}{2r_s}$	FRC elongation
A	$2\pi r_w\left(\frac{L_s}{2}\right)$	area of the first wall
V_0	$\frac{4}{5}\pi r_w{}^2\left(\frac{L_s}{2}\right)$	FRC plasma volume

3.3.5 Slowing down

The slowing down time is defined as the reciprocal of the Coulomb collision frequency between the fast moving ions with background electrons. This is equivalent to two times the reciprocal of the energy loss rate of fast ions to background electrons. The slowing down time in mathematical form is

$$\tau_s = \frac{3}{4}\frac{T_e^{3/2}}{z_i{}^2\sqrt{2\pi m_e}}\left(\frac{4\pi\varepsilon_0}{e^2}\right)^2\frac{m_i}{n_e\Lambda_e} \tag{26}$$

where the charge and mass of the ions refer to the fast ions and not the background ions. In terms of the units consistent with the code we get

$$\tau_s = \frac{0.2T_e^{3/2}m_i}{Z_i^2 n_e\Lambda_e} \tag{27}$$

The slowing down time of the fast ions is calculated inside the tauslow() routine.

3.3.6 Critical energy

When the energy of the fast ion is above the critical energy, the fast ion transfers most of its energy to the background electrons and when the energy of the fast ion is below the critical energy, most of the fast ion's energy goes into the background ions. The ecrit() routine calculates this critical energy. The equation for the energy loss of a fast-ion test particle is

$$\frac{dE}{dt} = -\sum_{\alpha=e,i} \nu_\varepsilon^{i/\alpha} E \ = -\frac{2E}{\tau_s}\left[1 + \left(\frac{E_c}{E}\right)^{3/2}\right] \tag{28}$$

where $\nu_\varepsilon^{i/\alpha}$ is the energy loss rate of a fast ion colliding with background species α, and E_c is the critical energy. The critical energy is

$$E_c = \left[\frac{3\sqrt{\pi}}{4}\frac{m_i^{3/2}}{n_e\sqrt{m_e}}\sum_i\left(\frac{n_i Z_i^2}{m_i}\Lambda_i\right)\frac{1}{\Lambda_e}\right]^{2/3} T_e \tag{29}$$

where m_i is again the mass of the fast ions and not the mass of the background ions. Simplifying the constants and putting in the proper units for the code, we get

$$E_c = m_i Te\left(\frac{56.96 Z_s \Lambda_i}{\Lambda_e}\right)^{2/3} \tag{30}$$

3.3.7 Fast energy fraction going to ions

A fast ion loses its energy as it slows down, and some of this energy goes into the background ions. Here we calculate the fraction of the fast ion's energy going into the background ions as is done in the ionfract() routine in the code. There are very few neutrals present in the system so we may neglect the loss of fast ion energy due to charge exchange. The fraction of fast ion energy that goes to the background ions is the ratio of the energy of the fast ion given to the background ions to the energy of the fast ion when it first born. We can write this as

$$f_{ion} = \frac{1}{E_0}\int_0^\tau dt\left(-\frac{dE}{dt}\right)\frac{\nu_\varepsilon^{i/\alpha}}{\sum_\alpha \nu_\varepsilon^{i/\alpha}} \tag{31}$$

where $\nu_\varepsilon^{i/\alpha}$ is the energy loss rate of species i to background species α. The birth energy of the fast ion is shown in Table 3-3. The time integral goes from zero to the time when the energy of the fast ion has slowed down to thermal energy and become part of the background distribution. We now perform the integral. An equivalent form for the fraction going to the background ions is

$$\begin{aligned}
f_{ion} &= \frac{2}{v_0^2}\int_0^{v_0}\frac{v_c^3 v}{v^3 + v_c^3}dv \\
&= \frac{2}{x_c^2}\int_0^{x_c}\frac{x}{x^3+1}dx \\
&= \frac{2}{x_c^2}\int_0^{x_c}\left[\frac{-1/3}{1+x} + \frac{1/3\left(x-1/2\right)}{\left(x-1/2\right)^2 + 3/4} + \frac{1/2}{\left(\frac{2x-1}{\sqrt{3}}\right)^2+1}\right]dx \\
&= \frac{2}{x_c^2}\left[\frac{1}{\sqrt{3}}\arctan\left(\frac{2x_c - 1}{\sqrt{3}}\right) + \frac{\pi}{6\sqrt{3}} - \frac{1}{6}\ln\left(\frac{x_c^2 + 2x_c + 1}{x_c^2 - x_c + 2}\right)\right] \\
&\equiv \frac{2}{x_c^2}gam(x)
\end{aligned} \tag{32}$$

The lower limit of the integral corresponds to the fast ion having no speed left after it has transferred all its energy. This is only an approximation since the fast ion slows down to as low as the background energy. Since the birth energy is very much larger than the background energy, our approximation introduces only a small error. The factor $gam(x)$ is evaluated in the gam() routine with $x = x_c$ being sent to the routine. Finally the fraction of the energy of the fast ion going into the electron is $f_{elect} = 1 - f_{ion}$.

3.3.8 Fusion reaction rate

The sigfus() routine calculates the fusion reaction rate in m^3/s. The reactions are identified in Table 3-2 and Table 3-6. The expression used for the reaction rate is

$$R_{i\sigma v} = \left[c_1 \Theta \sqrt{\frac{1}{T_{ion}^3 mc} \sqrt[3]{\frac{bg}{4\Theta}}} \right]^{-3\sqrt[3]{\frac{bg^2}{4\Theta}}} \tag{33}$$

where $\Theta = \dfrac{T_{ion}\left(1 + T_{ion}c_3 + T_{ion}^2 c_5 + T_{ion}^3 c_7\right)}{1 - T_{ion}c_2 - T_{ion}^2 c_4 - T_{ion}^3 c_6}$. Numerical values for $bg,\ mc,\ and\ \ c_1 \ldots c_7$ are shown in Table 3-6 and Table 3-7.

Table 3-6: Constants in Fusion Reaction Rate Equations.

Reaction	i	bg	$mc\ (10^6)$	$c_1\ (10^{-10})$	$c_2\ (10^{-3})$	$c_3\ (10^{-3})$
^{3}He(d,p)^{4}He	1	68.7508	1.124572	5.74129	4.15827	19.0541
D(d,n)^{3}He	2	31.3970	93.7814	0.054336	5.8577	7.68222
D(d,p)T	3	31.3970	93.7814	0.056718	3.41267	1.99167
T(d,n)^{4}He	4	34.3827	1.124656	11.7302	15.1361	75.1886

Table 3-7: Constants in Fusion Reaction Rate Equations (continued).

Reaction	i	$c_4\ (10^{-4})$	$c_5\ (10^{-4})$	$c_6\ (10^{-4})$	$c_7\ (10^{-6})$
^{3}He(d,p)^{4}He	1	2.45907	4.26442	0.0	7.13700
D(d,n)^{3}He	2	0.0	-0.0296400	0.0	0.0
D(d,p)T	3	0.0	0.105060	0.0	0.0
T(d,n)^{4}He	4	46.0643	135.000	-1.06750	13.6600

3.3.9 Fast ion pressure

The averfastpress() routine evaluates the volume averaged fast ion pressure in units of 10^{20} keV/m^3 summed over all reactions. The general form is

$$p_{fast} = \frac{2}{3} E_c \tau_s f(x_c) \int n_i n_j R_{i\sigma v} V' du \tag{34}$$

where $f(x_c)$ is evaluated in the gam() routine. The actual calculation for the local fast ion pressure is done in the fastionpress() routine. There is an extra factor of ½ for the D-D reaction in order to avoid double counting. The fast ion species involved are shown in Table 3-3. For 14.7 MeV protons and 3.67 MeV alphas from D-^{3}He and 3.52 MeV alphas from D-T reactions, we need to take the fast tail into account. The hot ion mode modifies x_c to $x_c = x_c \sqrt[3]{1 + n_\tau}$ and enhanced p_{fast} by a factor of $1 / (1 + n_t)^{5/3}$.

3.3.10 Energy confinement time

The energyconf_FRC() routine calculates the FRC energy confinement time, using one of four energy confinement time scalings. These are:

$$\tau_E = 1.3(10^{-5})\left(\frac{r_s^2}{\rho_{i0}}\right)^{1.35} \qquad \text{Hoffman scaling} \tag{35}$$

$$\tau_E = 1.3(10^{-5})(T_i + T_e)\left(\frac{r_s^2}{\rho_{i0}}\right)^{1.35} \qquad \text{modified Hoffman scaling} \tag{36}$$

$$\tau_E = 1.3(10^{-5})\, multiplier \left(\frac{r_s^2}{\rho_{i0}}\right)^{1.35} \qquad \text{multiplier scaling} \tag{37}$$

$$\tau_E = 483(10^{-9})\frac{length}{rw^{2/3}\, rs}\left(\frac{r_s^2}{\rho_{i0}}\right)^{1.2} \qquad \text{Ryzhkov scaling} \tag{38}$$

The ion gyroradius depends on the external magnetic field and the peak temperature. It is

$$\rho_{i0} = \frac{perpendicular \quad velocity}{cyclotron \quad frequency} = \frac{\sqrt{\dfrac{T_i}{\overline{\mu}}}}{\dfrac{(e) Z_{eff} B_e}{\overline{\mu}}} = 0.00323 \frac{T_i \overline{\mu}}{Z_{eff} B_c} \tag{39}$$

3.3.11 Particle confinement time

Currently the code has three particle confinement time scalings. These scalings are located in the particleconf() routine. The confinement scaling times are the Hoffman, the modified Hoffman, and a multiple of the energy confinement time:

$$\tau_p = 2.1(10^{-5})\left(\frac{r_s^2}{\rho_{i0}}\right)^{1.6} \qquad \text{Hoffman scaling} \tag{40}$$

$$\tau_p = 2.1(10^{-5})(T_i + T_e)\left(\frac{r_s^2}{\rho_{i0}}\right)^{1.6} \qquad \text{modified Hoffman scaling} \tag{41}$$

$$\tau_p = R_{tau} \tau_e \qquad \text{multiplier} \tag{42}$$

The ion gyroradius, ρ_{io}, is based on the external magnetic field and the peak temperature.

3.3.12 Hot-ion tail density

The taildensity() routine calculates the density of the fast deuteron tail. The tail density for D-^{3}He and D-T reactions respectively is

$$n_{tail}^{d3} = \frac{50.2\left(\frac{f_{elect} n_\tau}{1+n_\tau}\right)\tau_s \int n_2 n_3 Q_r R_{1\sigma v} V^{/} du}{2.257\left[\left(\frac{\left(\frac{3}{2}T_i\right)^{\frac{3}{2}} + E_c^{\frac{3}{2}}}{\sqrt{E_{tail}}} + \frac{3}{2}\sqrt{\frac{3}{2}T_i + E_{tail}}\right)\exp^{\left(-\frac{\frac{3}{2}T_i}{E_{tail}}\right)} + 3E_{tail} erfc\left(\sqrt{\frac{\frac{3}{2}T_i}{E_{tail}}}\right)\right]\int \frac{n_{prof}^2 V^{/}}{T_{eprof}^{\frac{3}{2}}} du} \tag{43}$$

$$n_{tail}^{dt} = \frac{62.5\left(\frac{f_{elect} n_\tau}{1+n_\tau}\right)\tau_s \int n_2 n_5 Q_r R_{4\sigma v} V^{/} du}{2.257\left[\left(\frac{\left(\frac{3}{2}T_i\right)^{\frac{3}{2}} + E_c^{\frac{3}{2}}}{\sqrt{E_{tail}}} + \frac{3}{2}\sqrt{\frac{3}{2}T_i + E_{tail}}\right)\exp^{\left(-\frac{\frac{3}{2}T_i}{E_{tail}}\right)} + 3E_{tail} erfc\left(\sqrt{\frac{\frac{3}{2}T_i}{E_{tail}}}\right)\right]\int \frac{n_{prof}^2 V^{/}}{T_{eprof}^{\frac{3}{2}}} du} \tag{44}$$

The value erfc() is the complementary error function. The complementary error function is approximated as

$$erfc(x) = \left[\frac{a_1}{1+p_0 x} + \frac{a_2}{(1+p_0 x)^2} + \frac{a_3}{(1+p_0 x)^3}\right]\exp\left(-x^2\right) \tag{45}$$

where *x* is the argument and the constants $p_0,\ a_1 \ldots$ are given in Table 3-8.

Table 3-8: Constants for Approximating the Complementary Error Function.

p_0	0.47047
a_1	0.3480242
a_3	-0.0958798
a_4	0.7478556

3.3.13 Charged particle fusion power

The WISC code accounts for the four main fusion reactions shown in Table 3-2. The fuspower() routine calculates the total charged-particle fusion power for the four reactions. The fusion power for each reaction is shown in Table 3-9. Note that each reaction has its own reaction rate despite the same notation. The total fusion power, p_{tot}, is the sum of these terms. The fast deuteron tail adds an additional term to the D-^{3}He and D-T charged-particle fusion power.

3.3.14 Fusion power going to electrons

The routine fuspowel() calculates the fusion power deposited into electrons. The power transfer to electrons from each ion species is shown in Table 3-10. The total fusion power going to the electrons, p_{elect}, is the sum of all these terms. The p_i's, where i is an integer from one to four, are found in Table 3-9.

Table 3-9: Formulas for Fusion Power.

Reaction	Formula	
^{3}He(d,p)^{4}He	$V_0 \langle \sigma v \rangle_1 Q_r \int n_2 n_3 V' du + V_0 \int n_{tail} n_3 Q_r R_{tail} V' du$	p_1
D(d,n)^{3}He	$V_0 \langle \sigma v \rangle_2 Q_r \int n_2 n_2 V' du$	p_2
D(d,p)T	$V_0 \langle \sigma v \rangle_3 Q_r \int n_2 n_2 V' du$	p_3
T(d,n)^{4}He	$V_0 \langle \sigma v \rangle_4 Q_r \int n_2 n_5 V' du + V_0 \int n_{tail} n_5 Q_r R_{tail} V' du$	p_4

Table 3-10: Fusion Power Deposited into Electrons.

protons from D-^{3}He reactions	$p_1 \left(1 - \frac{x_c + n_\tau}{1 + n_\tau}\right) \frac{E_1}{E_1 + E_2}$
alphas from D-^{3}He reactions	$p_1 f_{elect} \frac{E_2}{E_1 + E_2}$
^{3}He from D-D reaction	$p_2 f_{elect}$
protons from D-D reaction	$p_3 f_{elect} \frac{E_4}{E_4 + E_5}$
tritium from D-D reactions	$p_3 f_{elect} \frac{E_5}{E_4 + E_5}$
alphas from D-T reactions	$p_4 \left(1 - \frac{x_c + n_\tau}{1 + n_\tau}\right)$

3.3.15 Bremsstrahlung power

This bremsstrahlung() routine evaluates the bremsstrahlung radiation power with relativistic corrections. The power per unit volume with relativistic correction due to bremsstrahlung is

$$p_{brem}\left[\frac{MW}{m^3}\right] = 0.0053 n_e^2 \sqrt{T_e} \left[\begin{array}{l} z_{eff}\, ibrem1 + \left(0.00155 z_{eff} + 0.00414\right) T_e\, ibrem2 \\ +7.15\left(10^{-6}\right) z_{eff} T_e^2\, ibrem3 + 0.71 z_{2eff}\, ibrem4 \big/ \sqrt{T_e} \end{array}\right] \quad (46)$$

To get the total power we integrate over the volume. The ibrem's are routines calculating the profiles. We have

$$ibrem1 = \int n_{prof}^2 \sqrt{\gamma_{eprof}} V' du \tag{47}$$

$$ibrem2 = \int n_{prof}^2 \gamma_{eprof}^{3/2} V' du \tag{48}$$

$$ibrem3 = \int n_{prof}^2 \gamma_{eprof}^{5/2} V' du \tag{49}$$

$$ibrem4 = \int \gamma_{eprof}^2 V' du \tag{50}$$

3.3.16 Rotating magnetic field current drive power

The rotating magnetic field power current-drive (RMF power) is the power required to replace the magnetic energy dissipation caused by resistive friction. The expression for the RMF power is

$$\begin{aligned} p_{rmf} &= \int \eta j^2 dV \\ &= 7.958\left(10^6\right)\eta B_c^2 \sigma\kappa \int \frac{1+u}{\left(1-\sigma^2 u^2\right)\cosh^4\left[\frac{\kappa}{\sigma}\operatorname{arctan} h\left(\sigma u\right)\right]} du \end{aligned} \tag{51}$$

where j, and η are the current density and the resistivity respectively. The resistivity is the Spitzer resistivity and may be written as

$$\eta = \frac{3.257\left(10^{-9}\right) z_{eff} \Lambda_e}{T_e^{3/2}} \tag{52}$$

The RMF power from this formula is in the kilowatt range. The actual RMF power, however, including non-ideal effects, should be in the megawatt range. A parametric factor of 200 was arbitrarily added to get the RMF power into the megawatt range. The RMF power is calculated in the rmfcal() routine.

3.3.17 Synchrotron power

The synpower() routine calculates the power due to synchrotron radiation. The synchrotron power is believed to be very small in a low magnetic field and high beta system such as the FRC. There are no well-developed theories for synchrotron radiation loss for the FRC. Consequently we ignore the power loss due to synchrotron radiation in the FRC version. Zeroing out the synchrotron power is expected to give a small error.

3.3.18 Transport power

The charged particle transport power is evaluated inside the transport() routine. The transport power is simply

$$p_q = \frac{3V_0}{2} \frac{\int \left(n_i T_i + n_e T_e\right) V' du}{\tau_e} \tag{53}$$

This is the same as the thermal energy divided by energy confinement time.

3.3.19 Electron temperature

The electron temperature can be obtained from the electron power balance equation. The equation for electron power balance is

$$P_{ie} + P_{elect} + \left(1 - f_{inj}\right) p_{inj} = p_{syn} + p_{brems} + p^{e}_{trans} \tag{54}$$

where

$$p_{ie} = 0.247 Z_s V_0 \frac{n_e^2 \Lambda_e}{T_e^{3/2}} \left[T_i \int \frac{n_{prof}^2 \gamma_{iprof}}{\gamma_{eprof}^{3/2}} V' du - T_e \int \frac{n_{prof}^2}{\sqrt{\gamma_{eprof}}} V' du \right] \tag{55}$$

$$p_{inj} = p_{brems} + p_{syn} + p_q - p_{tot} \tag{56}$$

$$p^{e}_{trans} = \frac{0.024 n_e T_e V_0}{\tau_e} \left[\frac{n_0 T_i \int n_{prof} \gamma_{iprof} V' du + n_e T_e \int n_{prof} \gamma_{eprof} V' du}{\dfrac{n_0 T_i \int n_{prof} \gamma_{iprof} V' du}{R_{trans}} + n_e T_e \int n_{prof} \gamma_{eprof} V' du} \right] \int n_{prof} \gamma_{eprof} V' du \tag{57}$$

The various powers scale with the electron temperature as

$$p_{ie} = a \frac{\left(b T_{ion} - c T_e\right)}{T_e^{3/2}} \tag{58}$$

$$p_{syn} = a_s T_e^{5/2} \qquad \text{Trubnikov model} \tag{59}$$

$$p_{brem} = a_b \sqrt{T_e} \qquad \text{dominant term} \tag{60}$$

$$p^{e}_{trans} = a_t T_e \tag{61}$$

So we rewrite the electron power balance as

$$ac T_e - ab T_{ion} + T_e^{3/2} \left(a_s T_e^{5/2} + a_b \sqrt{T_e} + a_t T_e - p_{elect} - \left(1 - f_{inj}\right) p_{elect} \right) = 0 \tag{62}$$

This equation is solved for the electron temperature using a root finding routine. The coefficients are evaluated each time through the loop. The electron temperature is calculated in the eltemp() routine.

3.3.20 Density

The densityloop() routine calculates a self-consistent density of plasma species. These are then used to calculate the various power terms and electron temperature. The density of the various ion species is of the form $n_i = R_i n_2$ where R_i is shown in Table 3-11. The fractional change of the deuterium density is not allowed to be larger than the control constant z_{crit}. Other quantities, which densityloop also calculates, are shown in Table 3-12.

Table 3-11: Density Ratios.

i	R_i
1	$\dfrac{(10^{20})\tau_p\left(n_3\langle\sigma v\rangle_1 + \frac{1}{2}\langle\sigma v\rangle_3\right)}{\int n_{prof}V^{/}du}$
2	1
3	minimum of R_{hel} or $\dfrac{5(10^{19})\langle\sigma v\rangle_2}{\int n_{prof}V^{/}du + (10^{20})n_2\tau_p\langle\sigma v\rangle_1}$
4	$\dfrac{(10^{20})\tau_p\left(n_3\langle\sigma v\rangle_4 + n_5\langle\sigma v\rangle_4\right)}{\int n_{prof}V^{/}du}$
5	minimum of R_{trit} or $\dfrac{5(10^{19})\tau_p n_2\langle\sigma v\rangle_3}{\int n_{prof}V^{/}du + (10^{20})\tau_p n_2\langle\sigma v\rangle_4 R_{4\langle\sigma v\rangle}}$
6	$(1 + R_3 + R_5)f_i$

Table 3-12: Miscellaneous Density-Related Quantities.

Quantity	Formula
n_2 (beta limit)	$\dfrac{p_{allow}}{\sum_{i=1}^{6}\left(T_i\int n_{prof}\gamma_{iprof}V^{/}du + z_iT_e\int n_{prof}\gamma_{eprof}V^{/}du\right)R_i + \dfrac{p_{fast}}{n_2}}$
n_2 (fuel limit)	$\dfrac{n_{fix}}{(1 + R_3 + R_5)\int n_{prof}V^{/}du}$
$\langle n_e\rangle$	$n_e\int n_{prof}V^{/}du$
$\langle n_i\rangle$	$n_o\int n_{prof}V^{/}du$
β	$0.0402\left[\dfrac{n_0T_i\int n_{prof}\gamma_{iprof}V^{/}du + n_eT_e\int n_{prof}\gamma_{eprof}V^{/}du + P_{fast}}{B_c^2}\right]$

3.3.21 Edge plasma

The edge plasma thickness is approximated by

$$\Delta_{edge} = r_w - r_s\,, \tag{63}$$

which ignores end effects.

3.3.22 Blanket

The blanket thickness has been calculated to satisfy the simultaneous constraints of tritium breeding and heat transfer. The resulting blanket thickness is 0.7 m. The blanket volume and mass, which depend on the first-wall radius, are given by

$$V_b = \pi \; L \; (2\Delta_b r_w \;+\; \Delta_b^2) \tag{64}$$

and

$$M_b = \rho_b V_b \tag{65}$$

3.3.23 Shield

The shield thickness algorithm is

$$\Delta_s = \Delta_{s0} + \lambda_s \log_{10} \Gamma_n \,, \tag{66}$$

where Δ_s is the shield thickness, Δ_{s0} is the shield thickness for the reference wall loading, Γ_n=1 MW/m^2, and λ_s is the shield thickness for a 10-fold reduction in the neutron flux. The key criterion for this algorithm is that the full-lifetime radiation dose to the epoxy magnet insulators is less than 10^9 rads. The shield volume and mass are given by

$$V_b = \pi \; L \; (2\Delta_b r_w \;+\; \Delta_b^2) \tag{67}$$

and

$$M_b = \rho_b V_b \tag{68}$$

3.3.24 Magnets

The coil cross-sectional area is given by the ratio of the coil current to the coil current density:

$$A_c = \frac{I_c}{\bar{j}} \tag{69}$$

The coil current density is constrained to be below a maximum value, typically 50 MA/m^2. This value has been achieved in the LHD magnets with a peak magnetic field of 6.9 T at the coils and a maximum inner dimension of 3.9 m.[5]

3.3.25 Total radial build

The total radial build thickness is given by

$$\Delta_{tot} = \Delta_b + \Delta_s + \Delta_c + \Delta_m \tag{70}$$

3.3.26 Net power

The netpow(0) routine calculates the net electric power:

$$p_{net} = p_{gross} - p_{recirc} - p_{inj}/\eta_{eff} \tag{71}$$

The power flow appears in Figure 3-1. The various terms are shown in Table 3-13. The neutron wall load is also calculated. The wall load does not include the neutron energy multiplication factor. The neutron wall load is

$$\Gamma_{wall} = \frac{P_n^{dd} + p_n^{dt}}{A}. \tag{72}$$

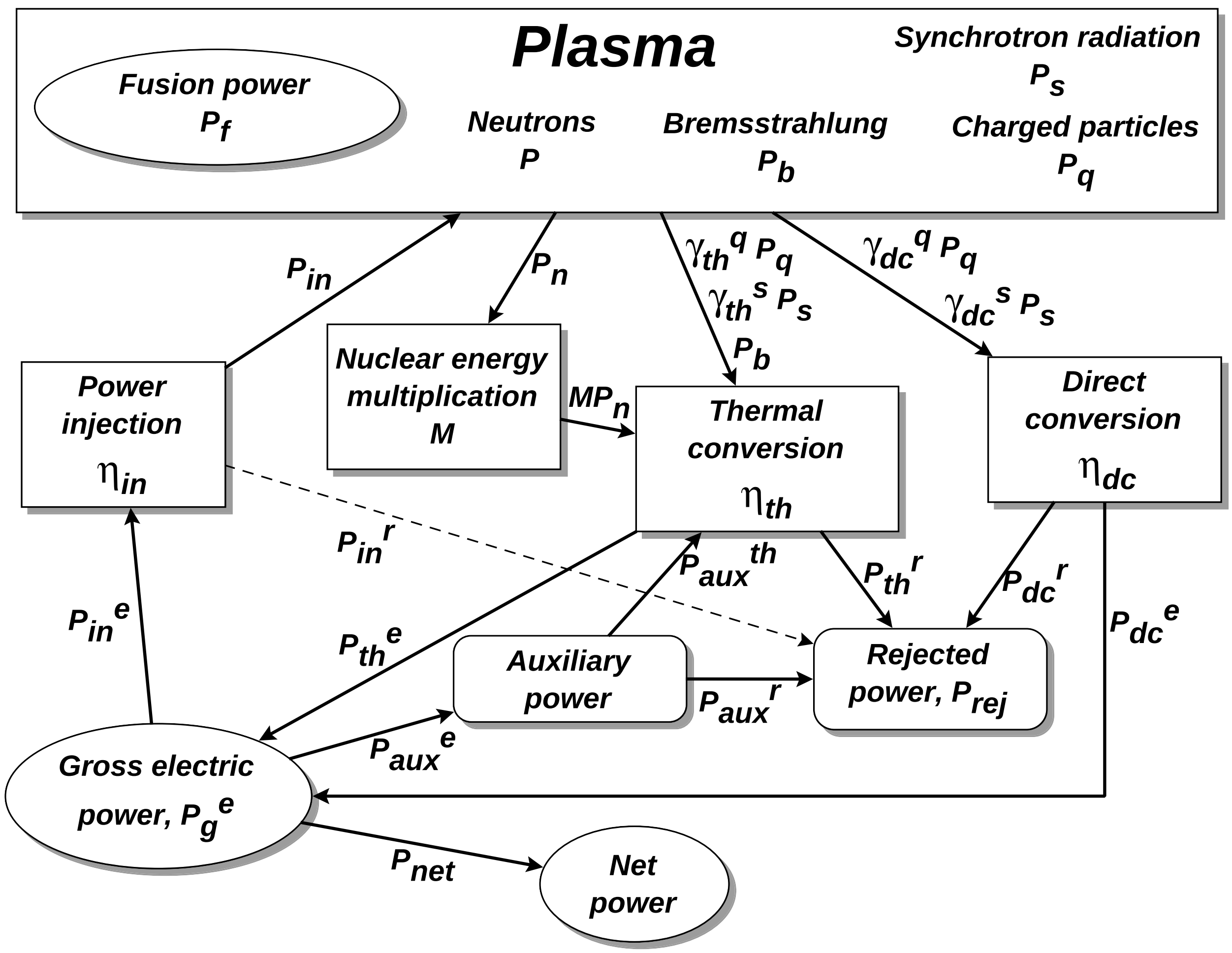

Figure 3-1: Plasma power flow for an FRC fusion power plant.

Table 3-13: Power Terms Used in Calculating Net Electric Power.

Quantity	Formula
p_{therm}	$p_{syn} + p_{brems} + p_q + M_{dd} p_n^{dd} + M_{dt} p_n^{dt} + p_{pump}$
p_{cryo}	$2\sqrt{(0.0017)\frac{B_e^2}{2\mu_0}\pi (r_w + sh)^2 L_s}$
p_{nuc}	$h_{mag} L_s$
p_{recirc}	$p_{cryo} + p_{nuc} + p_{pump} + p_{house}$
p_{gross}	$(k_{therm} = 0)$ $\eta_{syn} p_{syn} \frac{f_h}{f_h + (1 - f_h)(1 - \gamma_w)}$ $(k_{therm} = 1)$ $\eta_{syn} p_{syn} \frac{f_h}{f_h + (1 - f_h)(1 - \gamma_w)} + \eta_{therm}\left(p_{th} - p_{syn} \frac{f_h}{f_h + (1 - f_h)(1 - \gamma_w)}\right)$ $(k_{therm} = 2)$ $\eta_{therm} p_{th}$

3.3.27 Miscellaneous power

The miscpow() routine calculates various miscellaneous quantities such as the neutron power with the neutron energy multiplication factor. The ignition margin and the Q-value are, respectively,

$$igm = \frac{p_{tot}}{p_{brems} + p_{syn} + p_q} \tag{73}$$

$$Q = \frac{P_{fus}}{P_{inj}} \tag{74}$$

The system efficiency is

$$\eta = \frac{p_{net}}{p_{tot} + M_{dd} p_n^{dd} + M_{dt} p_n^{dt}} \tag{75}$$

3.4 References for Section 3

1. H.-S. Bosch and G.M. Hale, "Improved Formulas for Fusion Cross-Sections and Thermal Reactivities," *Nuclear Fusion* **32**, 611 (1992).

2. B.Q. Deng and G.A. Emmert, "Fast Ion Pressure in Fusion Plasmas," Fusion Technology Institute Report UWFDM-718, University of Wisconsin--Madison (January 1987).

3. J.R. McNally, Jr., "Physics of Fusion Fuel Cycles," *Nuclear Technology/Fusion* **2**, 9 (1982).

4. J.D. Huba, ed., "NRL Plasma Formulary," Naval Research Laboratory Report NRL/PU/6790—94-265 (1994).

5. O. Motojima, N. Yanagi, S. Imagawa, K. Takahata, S. Yamada, et al., "Superconducting Magnet Design and Construction of Large Helical Device," *Fusion Energy 1996, Vol. 3*, p. 47 (IAEA, Vienna, 1997).

4 Reference Case and APEX Liquid-Wall Cases

4.1 Reference case

Table 4-1 shows plasma and geometry parameters for the reference case of the present study. Table 4-2 shows engineering and power parameters for the study. If liquid walls prove possible, the power densities might reach even higher levels, as shown by Table 4-3 and Table 4-4, which were generated for the APEX study.[1] Note that the studies were done at somewhat different times, so various assumptions differ, notably the thermal efficiency.

Table 4-1: Systems Code Reference Case Plasma and Geometry Parameters for the D-T FRC Power Plant Engineering Scoping Study.

First wall radius, m	2
Separatrix radius, m	1.87
Separatrix length, m	20
Core plasma volume, m^3	220
First-wall area, m^2	251
Ion temperature ave., keV	24
Ion density ave., m^{-3}	1.5×10^{20}
Electron density ave., m^{-3}	1.7×10^{20}
Deuterium density fraction	0.47
Tritium density fraction	0.47
Alpha particle density fraction	0.04
Helium-3 density fraction	10^{-4}
Proton density fraction	10^{-4}
Impurity density fraction	0.01
Impurity Z	8
Zeff	1.6
γ for quasi-equilibrium	1.33
κ for quasi-equilibrium	0.69
σ for quasi-equilibrium	0.99
s	38
S*/E	14
Volume-averaged beta	0.56
Energy confinement time, s	1.1
Ash particle confinement time, s	2.3

Table 4-2: Systems Code Reference Case Engineering and Power Parameters for the D-T FRC Power Plant Engineering Scoping Study.

Vacuum magnetic field, T	2.4
Blanket thickness, m	1.45
Shield thickness, m	0.61
Cryostat width, m	0.05
Coil thickness, m	0.038
Ave. coil current density, MA/m^2	50
Coil stored energy, GJ	4.7
Neutron wall load, MW/m^2	5.7
Surface heat load, MW/m^2	0.12
Neutron power, MW	1427
Bremsstrahlung radiation power, MW	31
Charged-particle transport power, MW	367
Input power, MW	40
Fusion power, MW	1785
Ave. neutron energy multiplication	1.2
Total thermal power, MW	2114
Thermal conversion efficiency	0.52
Gross electric power, MWe	1099
Cryoplant power, MWe	35
Auxiliary power, MWe	53
Housekeeping power, MWe	10
Recirculating power fraction	0.090
Assumed plant availability	0.80
First wall and blanket mass, Mg (tonne)	1092
Shield mass, Mg	742
Magnet mass, Mg	170
Structure mass, Mg	301
Fusion core mass, Mg	2305
Mass power density, kWe/Mg	430
Net electric power, MWe	1000

4.2 APEX case

Table 4-3: Comparison of Systems Code Reference Case and APEX Case[1] Plasma and Geometry Parameters.

	This Study	APEX
First wall radius, m	2	2
Separatrix radius, m	1.87	1
Separatrix length, m	20	8
Core plasma volume, m^3	220	25
First-wall area, m^2	251	101
Ion temperature ave., keV	24	26
Ion density ave., m^{-3}	1.5×10^{20}	5.0×10^{20}
Electron density ave., m^{-3}	1.7×10^{20}	5.5×10^{20}
Deuterium density fraction	0.47	0.47
Tritium density fraction	0.47	0.47
Alpha particle density fraction	0.04	0.05
Helium-3 density fraction	10^{-4}	10-4
Proton density fraction	10^{-4}	10-4
Impurity density fraction	0.01	0.01
Impurity Z	8	8
Zeff	1.6	1.54
s parameter	38	16
S*/E	14	19
Volume-averaged beta	0.56	0.88
Energy confinement time, s	1.1	0.37
Ash particle confinement time, s	2.3	0.73

Table 4-4: Comparison of Systems Code Reference Case and APEX Case[1] Engineering and Power Parameters.

	This Study	APEX
Vacuum magnetic field, T	2.4	3.6
Blanket thickness, m	1.45	0.7
Shield thickness, m	0.61	0.84
Cryostat width, m	0.05	0.05
Coil thickness, m	0.038	0.057
Ave. coil current density, MA/m^2	50	50
Coil stored energy, GJ	4.7	3.3
Neutron wall load, MW/m^2	5.7	18
Surface heat load, MW/m^2	0.12	0.39
Neutron power, MW	1427	1844
Bremsstrahlung radiation power, MW	31	39
Charged-particle transport power, MW	367	464
Input power, MW	40	40
Fusion power, MW	1785	2307
Ave. neutron energy multiplication	1.2	1.2
Total thermal power, MW	2114	2730
Thermal conversion efficiency	0.52	0.40
Gross electric power, MWe	1099	1092
Cryoplant power, MWe	35	16
Auxiliary power, MWe	53	55
Housekeeping power, MWe	10	10
Recirculating power fraction	0.090	0.084
Assumed plant availability	0.80	0.80
First wall and blanket mass, Mg	1092	182
Shield mass, Mg	742	342
Magnet mass, Mg	170	101
Structure mass, Mg	301	94
Fusion core mass, Mg	2305	719
Mass power density, kWe/kg	430	1390
Net electric power, MWe	1000	1000

4.3 Reference for Section 4

1. R. W. Moir, T. D. Rognlien, K. Gulec, P. Fogarty, B. Nelson, M. Ohnishi, M. Rensink, J. F. Santarius, D. K. Sze, "Thick Liquid-walled, Field-reversed Configuration (FRC)," (prepared for ANS Topical Meeting on the Technology of Fusion Energy; thereby submitted to Fusion Technology, 2000).

5 Appendix: Key Papers Related to This Work

1. J.F. Santarius, G.A. Emmert, H.Y. Khater, E.A. Mogahed, C.N. Nguyen, L.C. Steinhauer, and G.H. Miley, “Field-Reversed Configuration Power Plant Critical Issues,” University of Wisconsin Fusion Technology Institute Report UWFDM-1084 (June 1998).

2. E.A. Mogahed, H.Y. Khater, and J.F. Santarius, “A Helium Cooled Li_2O Pebble Bed Blanket Design for Cylindrical Geometry,” (prepared for ANS Topical Meeting on the Technology of Fusion Energy; thereby submitted to Fusion Technology, 2000).

3. R. W. Moir, T. D. Rognlien, K. Gulec, P. Fogarty, B. Nelson, M. Ohnishi, M. Rensink, J. F. Santarius, D. K. Sze, “Thick Liquid-walled, Field-reversed Configuration (FRC),” (prepared for ANS Topical Meeting on the Technology of Fusion Energy; thereby submitted to Fusion Technology, 2000).

Preprint
UCRL-JC-139086

Thick Liquid-Walled, Field-Reversed Configuration

R.W. Moir, R.H. Bulmer, K. Gulec, P. Fogarty, B. Nelson, M. Ohnishi, M. Rensink, T.D. Rognlien, J.F. Santarius, and D.K. Sze

This article was submitted to
14th Topical Meeting on the Technology of Fusion Energy
Park City, Utah
October 15-19, 2000

September 22, 2000

U.S. Department of Energy

Lawrence
Livermore
National
Laboratory

THICK LIQUID-WALLED, FIELD-REVERSED CONFIGURATION*

R. W. Moir[a], R. H. Bulmer[a], K. Gulec[b], P. Fogarty[c], B. Nelson[c], M. Ohnishi[d], M. Rensink[a], T. D. Rognlien[a], J. F. Santarius[e], and D. K. Sze[f]
[a]Lawrence Livermore National Laboratory, P. O. Box 808, L-637, Livermore, CA 94550, Tel: 925-422-9808
[b]43-133 Engineering IV, Box 951597University of California, Los Angeles, CA 90024
[c]Oak Ridge National Laboratory, Oak Ridge, TN 37831-8218
[d]Kansai Univ, 3-35, Yamate-cho 3 chome, Suita-shi, Osaka, Japan
[e]University of Wisconsin, 1500 Engineering Dr. Madison, Wisc 53706
[f]Argonne National Laboratory, 9700 South Cass Ave, Bldg 207, Argonne, IL 60439

Abstract
A thick flowing layer of liquid (e.g., flibe—a molten salt, $Sn_{80}Li_{20}$ or Li —liquid metals) protects the structural walls of the field-reversed configuration (FRC) so that they can last the life of the plant even with intense 14 MeV neutron bombardment from the D-T fusion reaction. The surface temperature of the liquid rises as it passes from the inlet nozzles to the exit nozzles due to absorption of line and bremsstrahlung radiation, and neutrons. The surface temperature can be reduced by enhancement of convection near the surface to transport hot surface liquid into the cooler interior. The resulting temperature for evaporation estimates called, T_{eff}, is 660, 714 and 460°C for flibe, SnLi and Li, where thermal conductivity was assumed enhanced by a factor of ten for flibe. The corresponding evaporative flux from the wall must result in an acceptable impurity level in the core plasma. The shielding of the core by the edge plasma is modeled with a 2D transport code for the resulting impurity ions; these ions are either swept out to the distant end tanks, or diffuse to the hot plasma core. The calculations show core impurity levels adequately low for Li and $Sn_{80}Li_{20}$ but is about ten times too large for flibe. An auxiliary plasma between the edge plasma and the liquid wall can further attenuate evaporating flux of atoms and molecules by ionization. The current in this auxiliary plasma might serve as the antenna for the current drive method, which produces a rotating magnetic field.

1. Introduction

This paper analyzes the present understanding of a future power plant based on a field-reversed configuration (FRC) with a liquid first wall. Although expected to be unstable to ideal MHD modes, experimental FRC plasmas have proved to be relatively stable and robust. This may be due to shear flow or the finite ratio of plasma radius to average gyroradius (called s, see Table 1) in present experiments, which is one of several non-ideal MHD considerations that remain difficult to treat theoretically. In a fusion power plant, for example, the large gyroradii of the fusion products are also expected to contribute to stability. An FRC fusion core would have to have sufficient macroscopic stability to avoid excessive plasma energy losses. The main focus of this paper is on liquid wall features rather than plasma stability. Research teams at the University of Washington[1] and elsewhere are experimentally trying to use rotating magnetic fields to build up and sustain the FRC and see if the predicted high loss rates will nevertheless allow a practical power plant. The predicted power density is so high with the DT reaction that liquid walls are almost a necessity. Alternatives are to use the D^3He cycle as discussed in Ref. 2 or replace damaged first walls and structures often. The Astron power plant concept[3] was an early FRC that proposed using liquid walls.

This study is part of the (Advanced Power EXtraction) APEX[4] project, which is investigating innovative blanket concepts, with liquid wall systems as a major option. The underlying logic is to interpose a liquid of about 7 mean free paths for 14 MeV neutrons between the plasma and structures including the first wall so that these structures last the life of the plant. The structures satisfy the rough criterion that the damage should be less than 100 dpa (displacements per atom) and still fall within design specifications. It would be useful to develop a damage criterion versus liquid thickness for materials such as flow baffles that perform a reduced function (i.e., nonstructural function). The liquid is injected through chamber inlets as shown in Fig. 1 by nozzles that give the liquid enough azimuthal speed that centrifugal force keeps it against the wall even when the orientation is horizontal. Vertical orientation might have advantages and be necessary with liquid metals. The flow can be very nearly along field lines so that even liquid metals such as lithium or tin-lithium mixtures could work; however an important goal here is to see if the molten salt called flibe[5] (a mixture of LiF and BeF_2) will be workable. One of the virtues of flibe is its compatibility with stainless steel such as 304SS, if the chemistry associated with transmutation products can be controlled.
A set of typical FRC parameters is given in Table 1. Studies based on the tokamak configuration show the evaporation of the flibe, principally BeF_2 molecules, will overwhelm the burning plasma (put it out). However, the FRC can be different in that the edge plasma should not

a "gas box" from each end through an annular slot. The configuration is shown in Fig. 2.

The paper is organized as follows: Sec. 2 discusses the hydraulics of the wall flow. The inlet and outlet bulk liquid temperatures dictated by power conversion considerations are presented in Sec. 3, followed by an analysis of the liquid surface temperature in Sec. 4. The resulting evaporation rate of various liquids is given in Sec. 5, followed in Sec. 6 by calculations of impurity transport into the core from the wall vapor. The impact of liquid walls on current drive from rotating magnetic fields is discussed in Sec. 7, and conclusions and future work are given in Sec. 8.

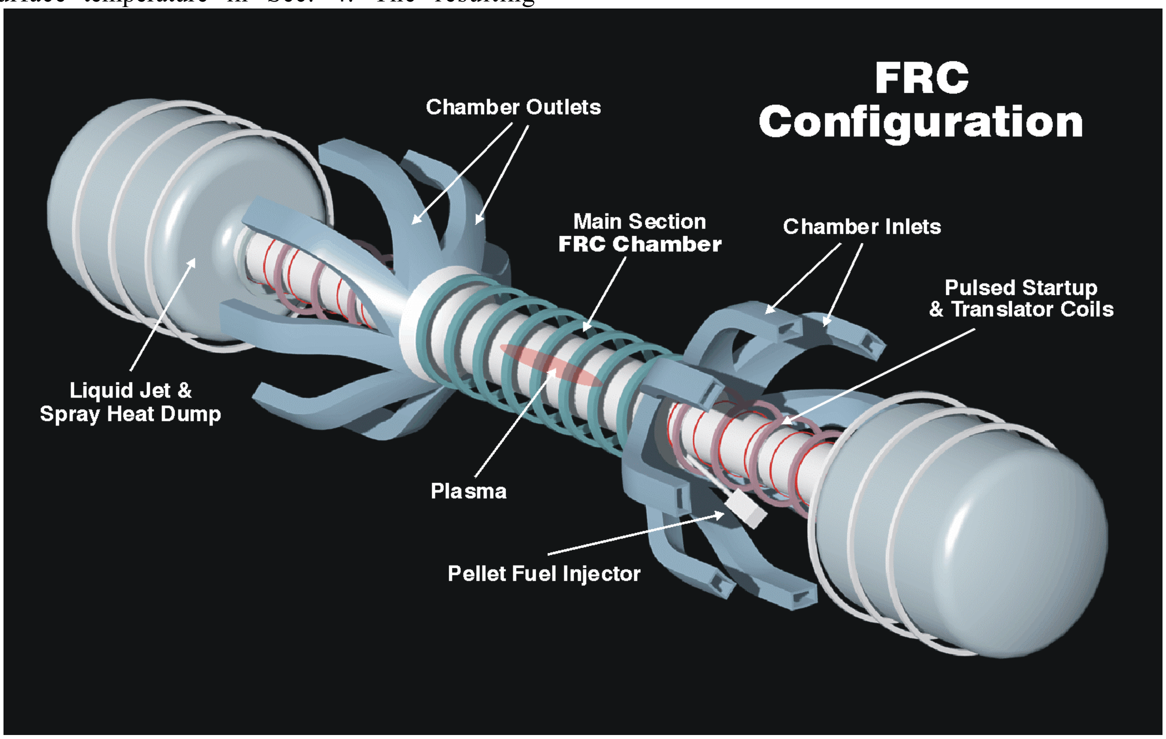

Figure 1. General layout of a FRC power plant design.

2. Hydraulics and the inlet and outlet nozzles

Hydraulics studies[4] using 3D computational fluid dynamics codes show the feasibility of providing the flow pattern called for in Fig. 3. Nozzle design will be challenging. The nozzles are exposed to neutrons so that their damage-limited lifetime needs to be determined. The inlet nozzle must not have excessive dripping that might cause core plasma contamination. Device orientation is important as vertical orientation, shown later in Fig. 8, could allow drips to miss the plasma in their vertical fall. The exit or receiver nozzles appear to be much more difficult. Splashing and choking will need to be strictly avoided. If the cross-sectional area of the exit nozzle is larger than that of the flowing liquid then choking might not occur. Once the flowing liquid is contained within the exit channel, it can be directed outside the chamber and then voids can be eliminated and the flow can be slowed down in a diffuser where its kinetic energy can be converted into potential energy (pressure=$0.5\rho v^2$). Vertical orientation will help in design of the exit nozzles and the diffuser. The acceleration-thinning problem in vertical orientation can be partially compensated by inserting flow baffles with the possible addition of azimuthal flow to prevent the flow over the baffles from entering the core plasma region. Another solution is to start with a thicker layer.

3. Mass flow and temperature diagram

We assume a 50 °C drop across the heat exchanger. This is a compromise, as we would like 100 °C. The HYLIFE-II heat transport system[6] assumes 100 °C drop across the heat exchangers, which are also the steam generators. The cost estimate for the heat transport system is 174 M$ out of a total direct cost of 1440 M$ for a 1 GWe plant and 338 M$ out of 2240 M$ for 2 GWe (1995$). If we assume a 50 °C drop will increase these costs by $2^{0.7}$ then the plant costs will increase by 7.5 and 9.5% for the 1 and 2 GWe plants, respectively. This is a large cost increase, which warrants further study. Our motivation is to reduce the surface

Table 1: Typical D-T FRC Power Plant Parameters.

	Liquid-Wall	Liquid-Wall	Solid-Wall	D^3He (ref. 2)
Liquid wall radius, m	1.5	2.0	2.0	2.0
Separatrix radius, m	0.39	1	0.88	1.1
Separatrix length, m	8	8	25	17
Core plasma volume, m^3	2.6	25	26	67
First-wall area, m^2	75	100	314	215
Average ion temperature, keV	12	18	13	88
Average ion density, 10^{20} m^{-3}	26	6.2	8.3	6.6, n_e
Peak ion density, 10^{20} m^{-3}	31	6.8	8.6	
Zeff	1.5	1.5	1.5	
s = plasma radius/ average larmor radius	7.5	26	4.3	9.2
Volume-averaged beta	0.97	0.78	0.90	0.9
Magnetic field, T	5.5	3.6	3.0	6.7
Energy confinement time, s	0.08	0.33	0.31	2.1
Ash particle conf. time, s	0.16	0.65	0.62	4.2
Neutron wall load, MW/m^2	27	18	6.4	0.4
Surface heat load, MW/m^2	1.7	1.2	0.236	1.7
Neutron power, MW	2000	1844	2000	80
Bremsstrahlung radiation power, MW	46	49	44	360
Line radiation @ 15% P_{alpha}, MW	78	69	70	
Charged-particle transport power, MW	415	383	426	1160
Input power, MW	40	40	40	
Fusion power, MW	2500	2306	2500	1600
Net electric power, MWe	1000	1000	1000	1050

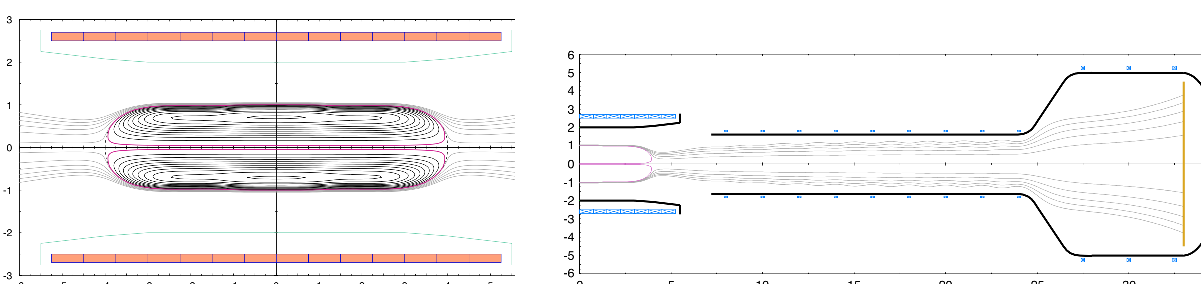

(a) (b)

Figure 2. FRC configuration. The magnetic flux surfaces from an MHD equilibrium calculation using the Corsica code are shown in (a) and the flux surfaces leading out to the end tanks are shown in (b).

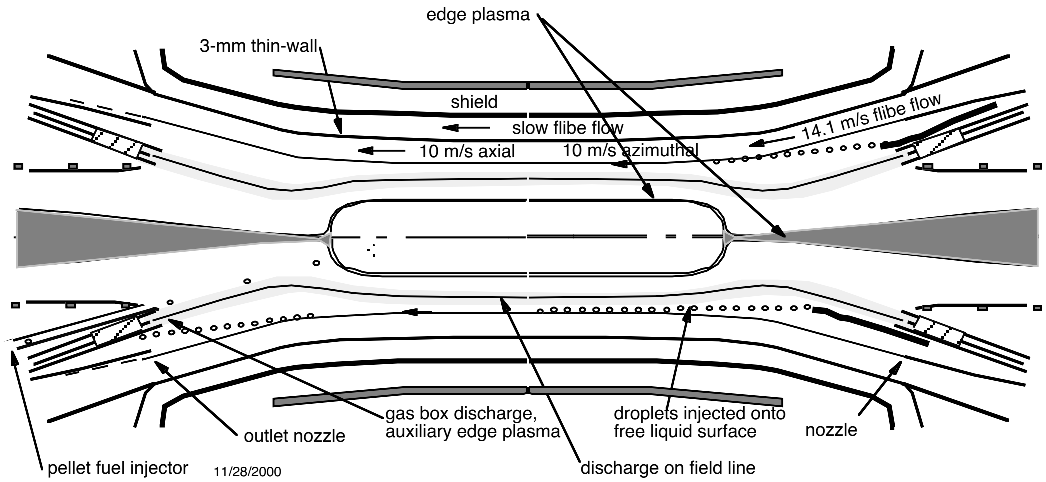

Figure 3. FRC showing the liquid flow, antenna current drive, gas box and pellet injector.

temperature to limit the evaporative flux, which is directed toward the core plasma. We assume the molten salt from the heat exchanger is mixed with the bypass flow to a mean temperature, 540 °C, which is then fed to the inlet nozzles. It might be possible to feed the 500 °C cooler molten salt from the heat exchanger directly to the nozzles feeding the surface flow. We assume a heat exchanger outlet temperature of 500 °C. This leaves 40 °C above the freezing temperature. In the future the melting point could be lowered by about 30 °C by reformulating the salt mixture; this would lower the salt temperature facing the plasma.

In order to arrive at 1000 MWe we assume a 2400 MW fusion power with blanket multiplication of 1.18. The blanket and charged particle power P is then 2750 MW. The volumetric flow rate and mass flow rates are:

$V' = \pi(2^2 - 1.5^2)\ 10\ \text{m/s} = 55.0\ \text{m}^3/\text{s}$

$m' = V' \times 2000\ \text{kg/m}^3 = 1.10 \times 10^5\ \text{kg/s}$

The temperature rise on average passing through the blanket, shield and end tanks is:

$\Delta T = P/m'C = 10.5\ °C$

C is the heat capacity. The mass flow rate to the heat exchanger is:

$m'P/\Delta TC = 2.31 \times 10^4\ \text{kg/s}$

If we take an axial flow speed of 10 m/s and a nominal 10 m/s azimuthal flow, then the power in the flowing liquid, which is a measure of the pumping power with no head recovery, is as follows:

$\text{Power} = 0.5 m'v^2 = 0.5 \times 1.1 \times 10^5\ \text{kg/s} \times (10^2 + 10^2)\ \text{m}^2/\text{s}^2 =$ 11 MW. The above parameters are shown in the mass flow diagram, Fig. 4. For the case of SnLi with the same thickness as flibe and 10 m/s flow along the field lines, we get a pumping power of 16.5 MW and assuming 100 °C across the heat exchangers we get the temperatures shown in parentheses in Fig. 4. The flow that bypasses the heat exchanger is 3.8 times that through the heat exchanger. It would be desirable to have all of the heat exchanger flow go to the blanket but then the flow speed rather than being 10 m/s would only be 2.7 m/s and the temperature rise discussed next would be very large resulting in high evaporation rates.

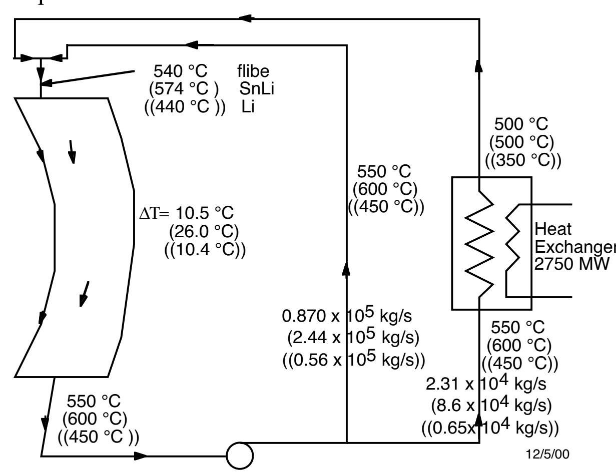

Fig. 4. Mass flow and temperature diagram for the FRC. The numbers shown are for flibe with the SnLi values shown in parentheses and Li, 1 m thick, in double parentheses

4. Heat transfer model and estimates of effective surface temperature

The temperature of the surface can be calculated once the heat load and the heat transfer characteristics of the liquid are known, by following a fluid element on the surface from the time it leaves a nozzle till it enters an exit nozzle. The complications are many. The radiation can be absorbed over a distance larger (deeper) than the thermal diffusivity distance x, which is the distance in a time, t, heat diffuses (x^2=tk/ρC). C is the heat capacity, ρ is the mass density, and k is the thermal conductivity. As an example, x = 0.47 mm for flibe, 4.9 mm for Li, and 4.2 mm for SnLi in 1 s. The mean free path for typical bremsstrahlung x-rays (15 keV) is 3 mm, 0.03 mm and 100 mm for flibe, SnLi and Li, so that volumetric heating (Eq.5) is used for flibe and Li but surface heating for SnLi (Eq. 4). In this case the surface temperature is less than if all the incident energy flux were absorbed on the surface. The other complication is the heat transfer can be greater for turbulent flow than for laminar flow. Heat conduction is a diffusive process. Reynolds analogy is the observation that mass transfer and heat transfer are analogous processes. Mass diffusion will carry heat when there is a temperature gradient just like heat is conducted (diffused). Mass transfer can be small due to molecular collisions or can be enhanced by the action of turbulent eddies. Steady heat conduction is governed by the equation:

$$P/A = k\,dT/dx \quad (1)$$

where P/A is the power flux striking the surface that penetrates a distance short compared to the thermal diffusivity distance mentioned above. Guided by Reynolds analogy, we argue that this equation can be modified to account for enhanced heat transfer by eddy motion.

$$P/A=(k+k')\,dT/dx \quad (2)$$

$$k_{eff} = k + k' = k\,(1+F) \quad (3)$$

The parameter F represents the enhancement of heat conduction due to turbulence; F = 0 gives the laminar limit. Magnetic fields tend to laminarize the flow, reducing F. Flow baffles can be added to create eddies or jets embedded in the liquid can enhance eddy motion which propagates to the surface; both will increase k_{eff}. Large values of k_{eff} might be possible with flibe where the electrical conductivity is so low that turbulence may play a large role. In the analysis to follow, F or k_{eff} is treated as a parameter because it is unknown; however, theoretical work by Smolentsev[7] and his planned experiments (e.g., flow baffles) should allow us to predicted k_{eff}.

Another idea to produce enhanced mixing (large k_{eff} values) is to spray droplets onto the surface. They must be small enough not to cause splash and large enough to cause persistent vortex motion. The idea and a relevant simulation[8] are shown in Fig. 5.

The temperature of the surface of the fluid element moving with the surface flow speed as we ride along as shown in Fig. 3 for a non-penetrating power flux P/A is then given by the equation

$$T = T_{inlet} + 2\,(P/A)\,(t/\pi\rho C k_{eff})^{0.5} \quad (4)$$

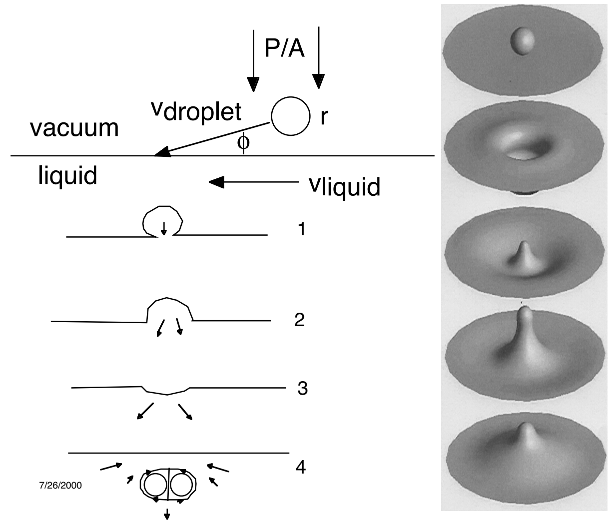

Fig. 5. The idea of droplets sprayed on a surface causing convection with no splash is shown on the left. A simulation is shown on the right with Reynolds number=2vr/ν =20 and Weber number=$\rho r v^2/\sigma$=2.

A key parameter is the incident power flux, P_{wall}/A, on the liquid surface. For the FRC we assume 3% of the fusion power of 2400 MW, or 78 MW, is non-penetrating line radiation which directly heats the surface which is 15% of the alpha power and may be low (20 to 40% is commonly assumed). With a surface area of 75 m^2, the P_{wall} (MW) /A (m^2) = 1.0 MW/m^2 . The temperature rise versus time is plotted in Fig. 6.

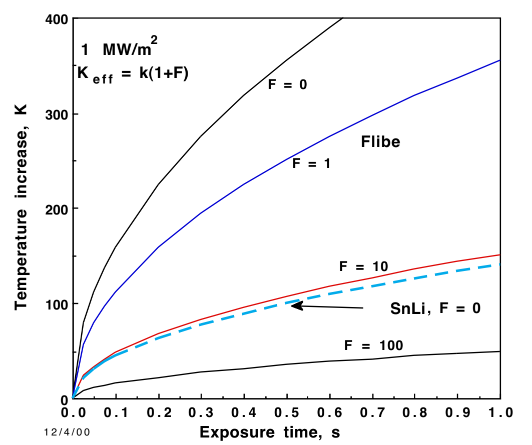

Fig. 6. Temperature rise of the fluid element versus time at 1.0 MW/m^2. F is the thermal conductivity enhancement factor to account for near surface turbulence or convection.

The surface temperature rise due to penetrating power flux due to neutrons and bremsstrahlung is given by

$$T = T_{inlet} + \frac{P}{V}\frac{\tau}{\rho c} \quad (5)$$

The temperature rise can be split into components.

$$\Delta T = T_{out} - T_{inlet} = \Delta T_{neutron} + \Delta T_{line} + \Delta T_{brem} + \Delta T_{cyclotron} + \Delta T_{particles\,on\,wall} \quad (6)$$

We include in Eq. 6 surface temperature rise due to cyclotron radiation and particle bombardment such as charge exchange neutrals, although we have neglected them in our calculations to date. The temperature rise in 0.8 s for flibe is 141 °C for line radiation, 34 °C for bremsstrahlung and 32°C for neutron heating and for SnLi is 131 °C for line radiation, 77 °C for bremsstrahlung and 70°C for neutrons heating. With an inlet temperature of 500 °C the outlet surface temperature is estimated at 707 and 780 °C for flibe and SnLi based on 1 MW/m^2 of line radiation and 0.6 MW/m^2 of bremsstrahlung radiation. For Li the temperature rise is 104 °C for line radiation, 2.4 °C for bremsstrahlung and 40 °C for neutron heating giving an outlet temperature of 500 °C for an inlet of 350 °C. Because the evaporative flux to be discussed in the next section is a very nonlinear function of temperature, one needs to average the flux along the wall. This averaging can be parameterized by the temperature T_{eff}, with $T_{eff} > T_{ave}$. The temperature to use in evaporation estimates called T_{eff} is 660 and 714 °C for flibe and SnLi and is 460 °C for Li.

5. Evaporation rates

Evaporation rates are used for the vapor source term in the edge plasma calculations to estimate the contamination of the core plasma by evaporation from the liquid wall. Evaporation from a surface into a vacuum is given by

$$J = \frac{n\bar{v}}{4}, \quad \bar{v} = \sqrt{\frac{8kT}{\pi m}}, \quad n = \frac{P}{kT}, \quad J = \frac{P}{\sqrt{2\pi mkT}} \qquad (7)$$

The density, n, is what would be present at equilibrium when evaporation equals condensation. In our case, where the edge plasma is close to the liquid surface and absorbs all evaporating particles that strike it, the density never reaches the equilibrium value but is one half of it. That is, all the particles are heading away from the liquid surface. When the edge plasma is not so close or when collisions occur, the equilibrium density is approached and condensation begins to cancel out evaporation. The concept of density away from equilibrium is not very useful, and we will emphasize evaporation rates (number of molecules leaving the liquid per square meter per second). This is the quantity that goes into the edge plasma calculation rather than either density or vapor pressure. From experimental data in the literature the equilibrium vapor pressure is given in Eq. 8, where T is in K and P is in Pa. The pressure can be converted from Torr to Pa via P(Pa) = 133.3×P(Torr). The dominant evaporating species is that given to the right of the pressure equation above. The BeF_2 density is 200 times LiF density. Li_3 will also be present. The flibe vapor pressure may be inaccurate since it is extrapolated from the data at 1000 °C. The evaporation rate of the various species is plotted in Fig. 7.

$$P(Pa) = \exp(25.63 - 24040/T) ......Li_2BeF_4 ....BeF_2 \ evaporation$$

$$P(Pa) = \exp(25.92 - 22540/T) ......LiBeF_3 .....BeF_2 \ evaporation \qquad (8)$$

$$P(Pa) = \exp(22.35 - 22300/T) ......Li_{17}Pb_{83} ....Pb \ evaporation$$

$$P(Pa) = \exp(22.16 - 17220/T) ......Li ....Li \ evaporation$$

$$P(Pa) = \exp(24.81 - 25800/T) ......Sn_{80}Li_{20} ....Li \ evaporation$$

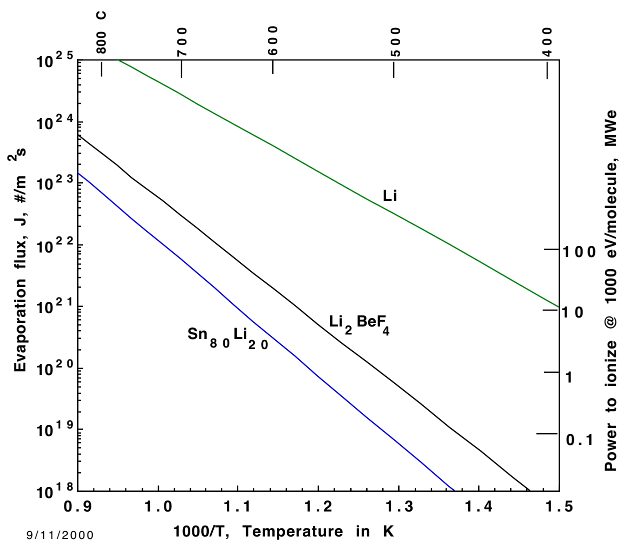

Fig. 7. Evaporation rates into vacuum for candidate liquids.

When evaporation becomes large, there are limiting effects, which will become important for liquid wall magnetic fusion configurations and especially for liquid divertors where the evaporation is very large. These effects are: (1)-collisional driven condensation of evaporated material, that is, evaporating molecules have collisions that return them to the liquid before they strike the edge plasma; (2)-evaporative cooling, and (3)-depletion of the volatile species at the surface. When condensation equals evaporation the latter two effects are absent. The first effect should start to become important above about 630 and 750 °C for flibe and $Sn_{80}Li_{20}$ and is expected to be especially important in the divertor. The second effect should be important for power fluxes of 1 MW/m^2 above about 920 °C for flibe. The third effect depends on molecular diffusion rates and turbulence and is never expected to be important.

The distance along the FRC edge is broken into zones with zone numbers assigned as shown in Fig. 8, and calculations are made for each zone with the evaporative fluxes shown in Fig. 7 with the results shown in Fig. 9. The configuration could be oriented either horizontally or vertically. For simplicity we assume the power is uniform over the cylindrical liquid wall from 4 m to -4 m at a radius of 1.5 m as listed in Table 1.

The transit time of the liquid is L/V = 8 m/10 m/s = 0.8 s. Again we emphasize this configuration is simplified for the sake of analysis but is representative of the phenomena involved.

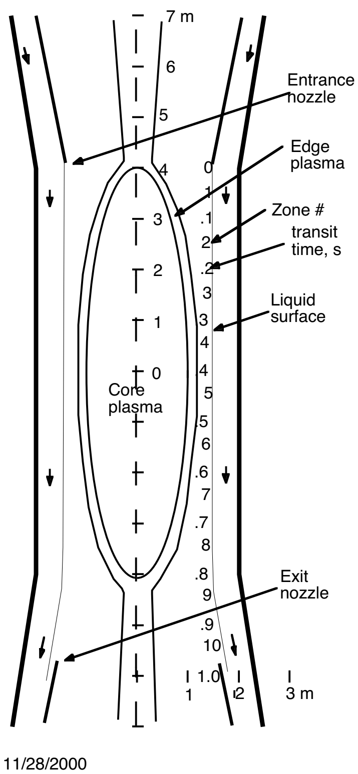

Figure 8. The FRC liquid flow model is shown. The flow path is in on one end and out on the other about 10 m in length.

Figure 9 shows the rapid variation of evaporation rate with distance. Tests from the impurity transport modeling presented in Sec. 6 show that the average evaporation rate along the wall is the important parameter. Thus, we define an effective temperature, T_{eff}, which gives the average evaporation. Because of the strong dependence of the evaporation on T (Fig. 7), T_{eff} is larger than T_{ave}. For example, if the outlet temperature from Fig. 7 is 700 °C and inlet is 500 °C, the average is 600 °C, the temperature, T_{eff}, to give the average evaporation is 640 °C.

6. Edge-plasma characteristics and impurity shielding

The plasma beyond the last closed magnetic flux surface is lost in an axial ion transit time out the end of the system, where it is assumed that the plasma escaping beyond the field-null region does not return from the large end-tank region. A balance between the axial loss and the assumed radial diffusion from plasma turbulence thus determines the radial thickness of the edge plasma. The edge plasma is especially important since it is responsible for shielding the core from the impurity vapor arising from evaporation of the liquid wall.

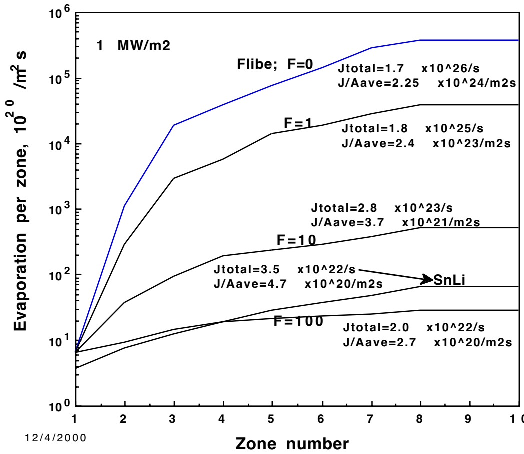

Figure 9. Evaporation per zone and total evaporation for FRC for 1 MW/m^2.

The plasma in the edge region is modeled by the two-dimensional plasma transport code UEDGE, which evolves equations for the plasma density, parallel ion velocity, separate electron and ion temperatures, and neutral gas density [9]. The code follows a DT fuel species, and each charge state of the impurity vapor that begins from the liquid side-wall as a neutral gas that then becomes ionized by the edge-plasma electrons.

Previously, UEDGE was used to assess the influx of impurities for a tokamak configuration [10]. For the FRC, there are two important differences: (1), the magnetic connection length along the B-field from the midplane to the effective end of the device (null-point region) is just the physical distance of ~ 4 m for our example, much shorter than for a tokamak which has a strong toroidal magnetic field, and (2), since the divertor plate is located very far from the null-point region, the return of plasma from recycled neutrals can be assumed to be small. In addition, the power density from this compact device is much larger, so that more energy flux is available at the edge to ionize impurities.

For the edge-plasma calculations in the scrape-off layer (SOL) beyond the magnetic separatrix, a slab geometry is used to approximate this thin annular region. In the axial direction, the SOL plasma contacts the core boundary along an 8 m length, followed by a 2 m exit region on each end to model flow into the long dump-tank region. The radial domain begins at the separatrix and extends radially for 2.5 cm; the vapor gas source flows in from the outer boundary for computational efficiency. The effect of moving the liquid wall farther away depends on the competing processes of converging fluxes and isotropizing collisions, but should not give very different results for the parameters of Table 1. The input parameters for the core plasma edge boundary are taken from Table 1. The edge density is assumed to be 0.1 of the core density, or $2x10^{20}/m^3$. The energy flux is a total of 20 MW/m^2, split equally between ions and electrons. The anomalous radial diffusion coefficients are 0.33 m^2/s for density and 0.5 m^2/s for the ion and electron energy; these values are simply taken from tokamak experiments.

The resulting calculated DT plasma parameters in the SOL are as follows: The radial decay length for the DT fuel density is 0.38 cm. The separatrix temperatures are Te=1.44 keV and Ti=1.50 keV. The radial decay lengths for the electron and ion temperatures are 0.43 cm and 0.60 cm, respectively, although the ion temperature shows a long plateau at about 0.5 keV.

The impurity gas is injected from the side wall into the DT edge plasma, and the new multi-species plasma equilibrium is calculated. The gas flux is taken as uniform in the axial direction; simulations with nonuniform injection to simulate the wall temperature profile shows the results are not very sensitive to this variation. The resulting impurity density at the separatrix on the midplane is shown in Fig. 10 for lithium (Li) from SnLi or Li and for fluorine (F) from flibe as the wall gas flux is varied. For Li, there is a break in the curve at about 2 x $10^{21}/m^2$ s where there appears to be a bifurcation in the solution as Te at the wall drops below ~1 eV. Also note that fluorine penetrates to the core boundary more easily than lithium, due, in part, to its higher ionization potential.

The tolerable amount of impurities in the core can be set by DT fuel dilution or by radiation loss. For impurities with low to moderate maximum charge state Z, dilution is the main concern. The fractional power reduction from dilution is given by $2Z\ n_z/n_{DT}$, where n_z and n_{DT} are the impurity and DT fuel densities, respectively [10]. Thus, a 20% power reduction for lithium (Z=3) and fluorine (Z=9), sets concentration limits of 0.03 and 0.01, respectively. Since the concentration levels of relevance are deep within the core, one can make one of two assumptions about impurity density variation in the core. The first is that the impurity density is flat with the same value as at the edge, and the second is that the impurity and DT densities vary together in the core such that the concentration remains a constant. These two assumptions give two limits to the operating points in Fig. 10, labeled (for F) 1% edge and 1% core. An argument for choosing the flat density case (1% core) is that the source of impurities is outside the core, but more detailed core analysis needs to be done.

The maximum allowable edge impurity densities shown in Fig. 10 give the corresponding gas flux limits from the wall. These gas fluxes can then be plotted on curves of wall temperature versus evaporative flux as shown in Fig. 11. These points thus identify the allowable wall temperature to prevent excessive impurity intrusion into the core plasma. The results correspond to the base case with no intervention techniques such as auxiliary heating in the edge plasma to help ionize the impurities well away from the separatrix boundary.

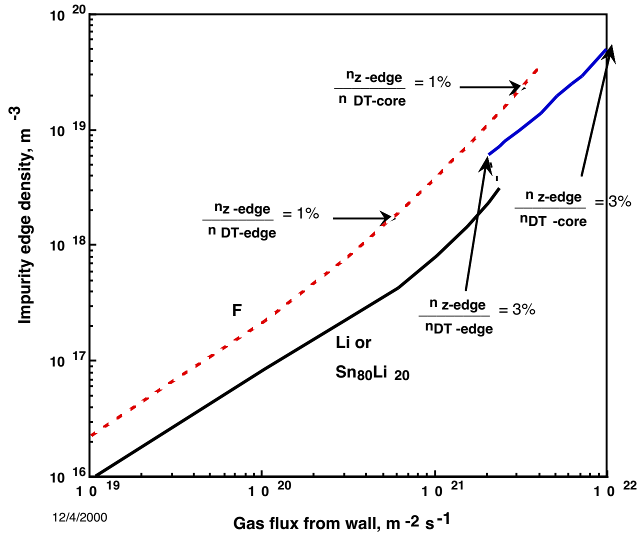

Fig. 10. Plot of impurity edge density vs average evaporation rate.

For flibe the effective temperature needs to be between 560 and 630 °C and for SnLi it needs to be between 660 and 720 °C, whereas we predicted in section 4, 660 and 715 °C for flibe and SnLi. For Li the effective temperature needs to be between 445 and 485 °C whereas in section 4 we predicted 460 °C.

7. Current drive by rotating magnetic fields

The importance of considering current drive is the complication of ports through the flowing liquid. One option for current drive to sustain the FRC is to use rotating magnetic fields[1,11]. It was first thought to drive current by locating antennae deep within the low electrical conductivity molten salt (5 mean free paths or more for 14 MeV neutrons). However, calculations show the skin depth at 32 kHz to be <<0.5 m. This means that too much power would be absorbed in the near field of the antenna, leaving little to drive and sustain the current. Next we studied antenna mounted on struts or end mounted to avoid penetrations through the flowing salt. The antenna would then be located between the FRC plasma (r~ 1 m) and the flowing wall (r~1.5 m). The antenna for the 0.39 m radius FRC produces a transverse field on axis of 0.02 T at a frequency of 125 kHz, and for the 1 m radius case, the field is also 0.02 T at a frequency of 24 kHz. The vapor density is $\sim 10^{19}$ to $10^{20}/m^3$, which is near the minimum in

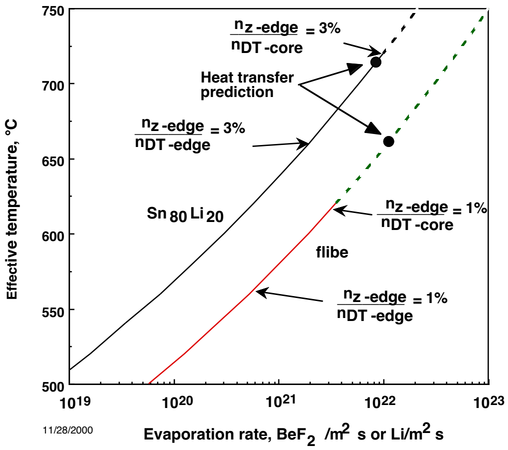

Fig. 11. Effecitve surface temperature versus evaporation rate where UEDGE says the core plasma is not overly contaminated with impurities. The dashed lines show where evaporation must be reduced by for example auxiliary edge plasma heating.

the Pachen breakdown curve, so discharges will easily occur. The question arises as to whether this plasma will prevent the field from penetrating outward from the antenna through the edge plasma. Apparently we do not need conductors along the field lines but rather we can rely on plasma discharge currents. Since we need to provide auxiliary power to the edge plasma to provide extra ionization and preventing or screen more of the evaporating liquid from entering the core plasma, we might as well use this discharge to drive the current that produces the rotating magnetic field for current drive. This concept of current drive will need future study to see if it is workable. Another option for current drive is to use the compact toroid (CT) fueling method.[12] Both methods avoid the need for ports penetrating the flowing liquid.

8 Conclusions and future work

We report on an initial iteration for a self-consistent design of a thick-liquid-protected FRC power plant. The most important concern, that of the evaporating liquid overly contaminating the core plasma has been addressed. For flibe the evaporation seems to be too much by about an order of magnitude forcing reliance on auxiliary shielding plasmas, condensation correction to evaporation and further enhancement of heat transfer near the free liquid surface. For SnLi and Li the evaporation seems to be tolerable by the plasma or close to it. We are encouraged to carry out further work in this promising area of liquid wall protection for fusion power plant design. There are a number of important issues that need further analysis. A short list of these follows:

1-include auxiliary edge plasma attenuation of evaporated wall material

2-study heat transfer enhancement methods to reduce the effective surface temperature and see if *F*=10 can be achieved by droplet spray, by vortex enhancing flow baffles or other means

3-study rotating field current drive by the auxiliary edge plasma discharge

4-consider the geometric effect of evaporation at 1.5 m with a plasma radius at 0.39 m and include the correction for condensation

9 Acknowledgements

*Work performed under the auspice of the U.S. Department of Energy by University of California Lawrence Livermore National Laboratory under Contract W-7405-Eng-48.

10. References

1. A. L. Hoffman, *et al.*, "The Large-s Field-Reversed Configuration Experiment," *Fusion Technology* **23,** 185 (1993).
2. H. Momota et al., “Conceptual design of the D-^{3}He reactor ARTEMIS,” Fusion Technology 21 (1992) 2307-2323.
3. N. C. Christofilos, “Design for a High Power-Density Astron Reactor,” J. Fusion Energy **8**, 97-105 (1989).
4. M. Abdou, APEX Interim report, UCLA-ENG-99-206 (1999). M. Abdou et al., Fusion Eng Design **54** (2001) 181-247.
5. The symbol for this molten salt in the past has been written as FLiBe but was made into a word with capital first letter in a fusion-spelling guide, Flibe. As usage has become more common lower case spelling has come into common use, flibe (pronunciation rhymes with tribe and scribe).
6. M. A. Hoffman and Y. T. Lee, “Performance and cost of the HYLIFE-II balance of plant,” Fusion Technology **21** (1992) 1557.
7. Sergei Smolentsev, M. Abdou, N. Morley, A. Ying and T. Kunugi "K-epsilon" Model of MHD Turbulence for Free Surface Flows, submitted to "International Journal of Heat and Mass Transfer" (2000).
8. Simulation by Damir Juric, Georgia Insittute of Technology, private communications 2000.
9. T.D. Rognlien, P.N. Brown, R.B. Campbell, et al. Contr. Plasma Phys., Vol. 34 (1994) 362.
10. T.D. Rognlien and M.E. Rensink, J. Nucl. Mater., to be pub. (2000).
11. M. Ohnishi, A. Ishida, Y. Yamamoto and K. Yoshikawa, “Current Sustainment of a Field-Reversed Configuration by Rotating Magnetic Field,” Trans. Fusion Technol. 27, 391 (1995).
12. Perkins, L.J., S.K. Ho, and J.H. Hammer, "Deep Penetration Fueling of Reactor-Grade Tokamak Plasmas with Accelerated Compact Toroids," *Nuclear Fusion* **28,** 1365 (1988).